Article

Not peer-reviewed version

Effect of Casting Shakeout Temperature on Residual Stresses of Hypoeutectic High Chromium Iron Alloys Using Hole-Drilling Method

Mbulelo Nggase * , Willie Nheta , Maje Phasha , Madzivhandila Takalani , Xiaowei Pan

Posted Date: 13 May 2025

doi: 10.20944/preprints202505.0918.v1

Keywords: high chromium alloys; hypoeutectic iron; residual stresses; casting shakeout temperature; hole-drilling method

 doi:10.20944/preprints202505.0918.v1

Article

Effect of Casting Shakeout Temperature on Residual Stresses of Hypoeutectic High Chromium Iron Alloys Using Hole-Drilling Method

M. Ngqase [1,*], W. Nheta [2], M. Phasha [3], T. Madzivhandila [1] and X. Pan [1]

[1] Faculty of Engineering and Built Environment, University of Johannesburg, P.O. Box 524, Auckland Park 2006, Johannesburg, South Africa

[2] University of Johannesburg, Mineral Processing and Technology Research Centre, P.O. Box 17011, Doornfontein 2028, Johannesburg, South Africa

[3] Advanced Materials Division, Mintek, Private Bag X3015, Randburg, Johannesburg 2125, South Africa

* Correspondence: ngqasembulelo@gmail.com

Abstract: Attention on residual stress (RS) development, magnitude, and distribution on abrasive wear materials, i.e., high chromium (Cr) iron alloys, has been minimal, even though these materials are prone to tearing or inferior mechanical properties because of distortion during manufacturing processes, such as casting and heat treatment, leading to premature failure of cast components. Identification of the source and succeeding management of RS provides an opportune possibility to enhance the product quality. In the current study, the as-cast hypoeutectic irons of ASTM A532, Type A, Class III, 25% Cr, i.e., sample A (S/A) and sample B (S/B), were cast at 1384 and 1390 degrees Celsius (°C) and allowed to solidify and cool for approximately 1645 and 1295 minutes (mins), respectively. Thus, the shakeout temperatures of S/A and S/B cast products were established to be approximately 60 and 180°C respectively. Resultant RS and macrohardness were determined at ambient temperatures using the hole-drilling method (HDM) and Brinell hardness (BH) tester machines, respectively. Higher hardness values of 600BHN were established on S/B compared to 526BHN for S/A. In addition, casting shakeout at higher temperatures, i.e., 180°C on S/B, yielded higher magnitudes of RS distribution compared to 60°C shakeout for S/A.

Keywords: high chromium alloys; hypoeutectic iron; residual stresses; casting shakeout temperature; hole-drilling method

1. Introduction

1.1. Background

High chromium (Cr) alloys are known as chromium white cast irons (HCWCI) alloys, which are extensively used as abrasion wear materials in the comminution processes, such as crushing, grinding, and milling industries, as well as in the handling of abrasive materials, such as mineral ores in both dry and wet environments. Grinding balls are commonly used during ore comminution. However, comminution itself is a critical process used during mineral processing, power plants, cement production, and pharmaceutical industries [1–3]. HCWCI alloys are due to substantial Cr additions added as one of the general carbide formers to cast irons. Thus, creating numerous types of carbides, i.e., M_3C, M_7C_3, and $M_{23}C_6$ [1–6] based on various Cr-levels added into the liquid iron to improve hardness, corrosion, and establishing M_nC_m-type of carbides and abrasive wear resistance [2,3,7].

Higher Cr-levels improve corrosion resistance and alter carbide morphology. Impact energy, i.e., fracture toughness of the iron, depends on many various aspects, such as resultant retained austenite (γ-Fe) and carbon (C) content in the γ-Fe or martensite (α-Fe) phase and destabilisation heat treatment temperatures, etc. [1–10]. Thus, the mechanical properties of the high Cr-irons are governed

 doi:10.20944/preprints202505.0918.v1

by both the ferrous matrix structure and carbides, i.e., Cr-rich carbides [1,2,4,7–10]. Furthermore, during hypoeutectic and hypereutectic iron solidification and cooling of high Cr-irons, γ-Fe and M_7C_3, respectively, are the primary phases to nucleate, followed by subsequent simultaneous nucleation of eutectic constituents as shown in Equation 1 (Eq. 1) below, consisting of both γ-Fe and Cr-rich carbides, i.e., M_7C_3-type of carbides. In eutectic irons, both γ-Fe and M_7C_3 nucleate simultaneously during solidification and cooling [1,4–6,8–10].

$$L > \gamma Fe + (Cr, Fe)_7C_3/M_7C_3 \quad (1)$$

where γFe = γ-Fe

Nonetheless, for casting components normally hypereutectic irons are avoided due to the nucleation of primary carbides and a higher volume fraction of carbides, i.e., a carbide volume fraction (CVF), leading to a higher rejection or scrap rate due to fine cracks usually observed after the casting shakeout or knockout process. Hypoeutectic and eutectic irons of HCWCI are generally cast for engineering components as abrasive wear materials [1,4,7–11]. Due to the lessening of both C and Cr contents from the ferrous matrix, i.e., γ-Fe in hypoeutectic irons, liquid iron is enriched in both C and Cr, reaching a eutectic reaction as shown in Eq. 1, and the eutectic constituents nucleate simultaneously. The martensite start (M_s)-temperature of the iron is increased above ambient temperatures, i.e., ≤ 25°C. Thus, α-Fe at the periphery of eutectic M_7C_3 type of carbides is established with a minimum volume fraction as compared to the primary phase, i.e., primary γ-Fe in hypoeutectic irons [1,4,7,10,11]. While in hypereutectic, liquid iron is getting deprived of both C and Cr-content due to the primary nucleation of M_7C_3-type carbides leading to a eutectic reaction taking place, resulting in the formation of eutectic constituents as shown in Eq. 1-1 [1,4–12].

Eutectic constituent precipitation stops before reaching minimum eutectic temperatures, i.e., the end of the eutectic reaction [11]. Hutchings and Shipway (2017), cited by Tupaj et al. [13], noted that resistance to abrasive wear is normally the main fundamental criterion for material selection for engineering parts and/or components. The exceptional resistance to abrasive wear is due to a higher volume fraction, i.e., CVF of hard Cr-rich carbides, which is estimated from Eq. 2 below. On the other hand, the metallic matrix (M), i.e., retained γ-Fe plus α-Fe of the iron, contributes to the material's toughness [11–14], which can be estimated from Eq. 3 below [12–14].

$$CVF\ (\%) = 12.33\ wt.\%C + 0.55\ wt.\%Cr - 15.2 \qquad std.dev. \pm 2.11 \quad (2)$$

$$\mathrm{M}\ (\%) = 100 - CVF \quad (3)$$

High nominal concentrations of Cr-additions lead to higher Cr/C ratios, i.e., ≥ 6.5 [13] in cast irons, and aid to avoid and suppress graphite and pearlitic nucleation while stabilising higher volumes of γ-Fe and hard Cr-rich carbides, i.e., M_7C_3-type carbides. In addition, hardening-alloying elements, i.e., copper (Cu), manganese (Mn), nickel (Ni), and molybdenum (Mo), are typically added to overcome the formation of pearlite during solidification and cooling processes [2,3,5–10,14]. Islak et al. [4] cited that the impact properties of HCWCI alloys are supported upon microstructural balance among the γ-Fe ferrous matrix, i.e., the volume fraction that will be altered to the α-Fe ferrous matrix and carbides. It should be noted that increasing both C and Cr contents of the high Cr-irons increases CVF while reducing interdendritic structure. However, reducing both C and Cr-contents of the alloy increases the ferrous matrix volume fraction, thus increasing the interdendritic structure, which promotes carbide precipitation [1–14].

1.2. Development of Residual Stress Within Cast Irons

Residual stresses (RSs) are largely predictable during casting processes due to uneven cooling rates, phase transformation, and expansion and contraction restriction of casting parts, especially complex shapes due to cores and sand mould restrictions [15–18]. In addition, RSs can also exist in the absence of any thermal gradients and/or external forces [16,19–21]. Thus, RSs can be described as

 doi:10.20944/preprints202505.0918.v1

stresses that remain in the interior of a body of a component and/or casting that are due to non-uniform temperatures, i.e., temperature gradients, and other interior cultivators that result from the manufacturing processes of cast components, especially metal components [14,22–25]. As a result, the origins of RSs can be categorised as chemical, thermal, or mechanical [26–30]. Since high Cr-irons, i.e., HCWCI alloys, are manufactured through casting processes, this study only covers both mechanically and thermally induced RSs on macroscopic and microscopic levels. Thus, mechanically induced RSs, which relate to manufacturing processes, result in uneven plastic deformation [16,31–33]. Thermally induced RSs relate to non-homogeneous heating and/or solidification and cooling on an infinitesimal level as a result of diverse coefficients of thermal expansion (CTE) amongst various constituents and microstructural phases [16,34–37].

Mohamed et al. [34] reported that several factors are well known for causing RSs, and these stresses are due to the establishment of distortion gradients in various casting parts as a result of variances in loading and/or solidification rates, phase changes, or modifications in the CTE of the phase presence in the iron. During casting processes, casting components are normally exposed to internal and external manacles and/or constraints when solidifying and cooling, respectively. Thus, leading to irregular distribution of strains and subsequently RSs. Interior restrictions depend on variances in cooling rate through various casting components, resulting in irregular contractions. Cooling after solidifying and solid-state transformation causes variances in shrinkage [38–40]. However, external constraints result from casting profiles and the amount of the material that contracts and restructures, whereas solidification and cooling relate to the sand mould properties [16,41–44]. Furthermore, Kainer (2003), cited by Lundberg & Elmquist [45], noted that entire thermal contractions are generally related to lessening temperatures and altering conditions of the iron's microstructural constituent through thermal stress experienced during casting processes. Thus, thermal stresses encompass various significances, i.e., distortion, cracking, and RS [16,45–51].

2. Material and Methods

2.1. Melting and Casting Processes

AW charge material of HCWCI alloy, i.e., hypoeutectic compositions from ASTM A532, Type A, Class III, 25%Cr, were melted and cast using 4 tonnes (t) industrial induction furnace and ladle equipment, respectively. Thus, Table 1 below shows casting limits, i.e., casting parameters during sample preparation, such as casting, solidification, and cooling processes as well as the shakeout process. Furthermore, Figure 1 below shows the gross casting weight (GCW) of the experimental and special casting components, i.e., the stress lattice casting component design for complete and sound stressed casting of the HCWCI alloy.

Table 1. Casting and shakeout process parameters.

Casting Parameters	Casting Identity Number (CId)	
	S/A	S/B
Melting Temperature (T_M) in ^oC	1480.00	1480.00
Casting Temperature (T_C) in ^oC	1384.00	1390.00
Casting Shakeout Temperature (C_{ST}) in ^oC	60.00	180.00
Knockout Period (C_{KP}) in minutes (mins)	1645.00	1295.00
Pouring Time (P_T) in seconds (secs)	22.00	23.00
Gross Casting Weight in Kilograms (kg)	114.28	113.48
Net Casting Weight in Kilograms (kg)	90.16	88.25

 doi:10.20944/preprints202505.0918.v1

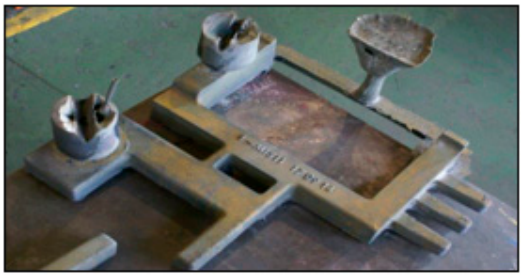

Figure 1. Experimental lattice casting component after casting shakeout process, i.e., GCW.

Special casting design presents asymmetrical shapes, and the cooling of special stress lattice castings are irregular. The determination of the design stress lattice shape is that of contraction of the interior and external sections of the cast component, which are highly restricted due to various core sizes and sand mould through cooling processes. Additionally, irregular cooling of the stressed lattice casting leads to various temperature gradients due to various casting section thicknesses. Whereas cores and moulds are further imposing a higher degree of restraint towards the casting during solidification and cooling, thus casting components are released, i.e., the casting shakeout process from the mould with RS distribution.

2.2. Experiential Procedures

2.2.1. Chemical Composition

The chemical composition of the liquid iron during the melting process before casting was accomplished by means of chill-cast moulds. General standard procedure for grinding casting coupons flat using 60 grit paper was used, whereas optical emission spectrometer (EOS), i.e., Specromaxx-type of spectrometer, was used to perform the chemical analysis. Additionally, chemical analysis of the liquid iron was validated through performing chemical analysis of the casting components after casting shakeout and knockout, respectively. Thus, more than three tests were performed, and an average was recorded.

2.2.2. Hardness Evaluation

Macrohardness, i.e., the bulk hardness measurement of the casting, was performed at ambient temperatures through a Brinell hardness tester machine. Random casting areas were selected for grinding before the hardness test measurement. A load of 750kg was used, whereas five indentations were performed, and an average value was recorded.

2.2.3. Residual Stress Measurements

The hole-drilling method (HDM), i.e., the SINT Technology RESTAN MTS-3000 RS measuring device, was used to measure RS in the hole-drilling strain-gauge (HDS) technique of the stress reduction "*relaxation*" technique. The HDM uses ASTM standard E837, which depends on stress comparison when a hole is bored "*drilled*" at the midpoint of a rosette strain gauge. Additionally, iron's properties and RS measurement procedure relate to strain relaxation measured at two dissimilar surfaces, i.e., P1 and P2, as shown in Figure 2 below. While the elastic properties of HCWCIs used for RS calculation were approximated to be approximately 216 GPa and 0.291 for Young's modulus and Poisson's coefficient, respectively. Thus, the HDM measures the direction and the magnitude of the principal stresses, whereas the measurement was performed at ambient temperatures. The HDM procedure is simple and is summarised into seven uncomplicated steps. For more information and understanding on the HDM preparation, the following publications are recommended [14,52–58]. RS measurement was computed by means of strain data and formulas cited in ASTM E837-08.

 doi:10.20944/preprints202505.0918.v1

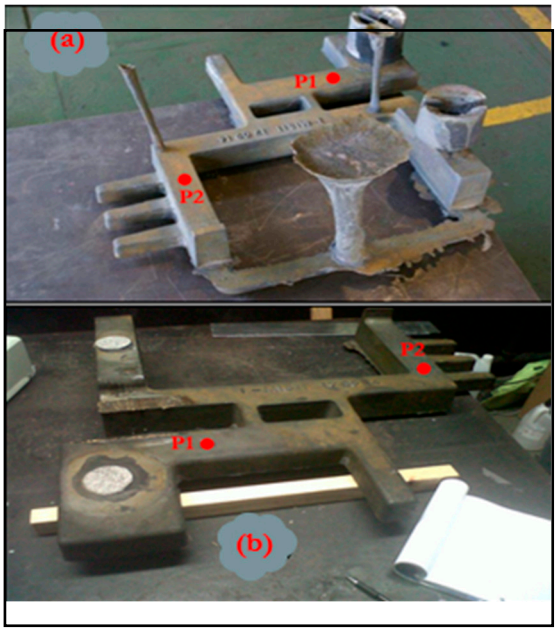

Figure 2. Experimental lattice casting design, i.e., (a) GCW and (b) NCW, respectively.

Furthermore, Figure 2 offered experimental stressed castings in GCW [Figure 2a] and net casting weight (NCW) [Figure 2b], respectively, in as-cast condition. GCW denotes comprehensive casting before removal of junk materials, i.e., pouring cup, sprue, risers/feeders, ingates, and vents to yield the NCW. While the latter is the saleable or actual casting component after the removal of junk materials, i.e., the net casting component, i.e., NCW. Drill bit cutters coated at the tip and/or end mill with tungsten carbide material at a speed of approximately 300 000rpm (revolutions per minute) through an air turbine were used to avoid generating any RS because of the drilling technique introduced to the iron. Thus, awareness of the extent and distribution of RSs is principally important to ensure the safety of the operation during material application.

3. Results and Discussion

3.1. Chemical Analysis

Prepared experimental alloys of high Cr-iron coupons of hypoeutectic composition were analysed in cross-sectional area(s) for chemical composition using OES, and the chemical composition is presented and summarised in Table 2 below. It is observed that the actual chemical composition of the experimental alloys agrees with ASTM A532, Type A, Class III, 25%Cr. Phosphorus (P) in the S/B casting component is slightly out of specification, i.e., 0.004 *wt.* %P than the recommended concentration in the ASTM A532, Type A, Class III material standard. However, 0.004 *wt.* %P is a small amount and can be disregarded, since P is a trace element; thus, there will not be any effect due to this excess amount. Trace elements are normally those elements or impurities that are detected within alloys but are not having any impact or effect. Thus, the chemical composition of S/A and S/B substantiates that they are those of the hypoeutectic composition of the HCWCI alloy. As estimated from Eq. 2, the computed CVF of the experimental castings, i.e., S/A and S/B cast products components, are approximately 28.87 and 32.19% CVF, respectively, of eutectic carbide type, i.e., M_7C_3 plus secondary carbides, i.e., $M_{23}C_6$ carbide type [7,9,10,14,15].

Table 2. Cast chemical analysis of experimental heats of ASTM A532, Type A and Class III.

Element	Composition (*wt. %*)	Casting Identity Number (CId)	
		S/A	S/B
C	2.0–3.3	2.50	2.70
Si	≤ 1.50	0.60	0.73

 doi:10.20944/preprints202505.0918.v1

Mn	≤ 2.00	0.66	0.66
S	≤ 0.100	0.054	0.075
P	≤ 0.060	0.026	0.070
Cr	23.0–30.0	24.09	25.65
Mo	≤ 3.00	0.19	0.17
Ni	≤ 2.50	0.36	0.44
Cu	≤ 1.20	0.20	0.12
Fe	bal.	71.00	69.00
CVF (%)		28.87	32.19
Cr/C Ratio		9.6	9.50

Furthermore, the volume fraction of the ferrous matrix, i.e., γ-Fe plus α-Fe, is computed using Eq. 3 and is approximately 71.13 and 67.81% in S/A and S/B cast products, respectively. It should be noted that Cr/C ratios of S/A and S/B cast products are computed as 9.6 and 9.5, respectively. According to Tupaj et al. [13], pearlite transformation is not possible since Cr/C ratios of experimental alloys are greater than 6.5. Thus, the resultant metallic matrix constitutes the maximum and minimum volume fractions of γ-Fe and α-Fe, respectively [59,60].

3.2. Hardness Evaluation

Hardness measurements of S/A and S/B cast products were established to be approximately 526 and 600HBN, respectively, compared to 450BHN for ASTM A532, Type A, Class III material standard, i.e., 25%Cr [14]. The obtained hardness values are higher than the hardness values presented in ASTM A532, i.e., hardness requirements. Thus, established higher hardness estimates are due to 60 and 180°C casting shakeout temperatures on S/A and S/B cast product components, respectively, coupled with higher values of %CVF. Furthermore, an increase in hardness values from S/A to S/B castings is noticed from an increase in C from 2.5 to 2.7 *wt.* %, 24.09 to 25.65 *wt.* %Cr, and 28.87 to 32.19% CVF. Seidu et al. [61] in their studies established that prolonging casting shakeout times, i.e., knock-off times, lessens hardness, thus raising the carbide grain size. Ferrous matrix is reduced from 71.13 to 67.81%, as C and Cr-content are increased from 2.5 to 2.7 *wt.* % and 24.09 to 25.65 *wt.* %Cr on S/A and S/B cast products, respectively. This has led to the enhancement of hardness, which is influenced by higher CVF, i.e., 28.87 to 32.19% of the total Cr-rich carbides, i.e., M_7C_3/ $(Cr, Fe)_7C_3$ type of carbides within the iron structural composition [10,62,63].

Additionally, higher casting shakeout temperatures (C_{ST}), i.e., 60 and 180°C (as summarised in Table 1), with reduced metallic matrix content have contributed to higher hardness values. During the casting process, i.e., pouring, solidification, and cooling processes, various casting parameters, such as fracture toughness, hardness, RSs, etc., are influencing the final casting quality. An improved understanding of the casting process is normally beneficial to analyse for process improvement. Thus, the mechanical aspects of the RS in the casting components are driven by thermal gradients, which are due to heat transfer from the part to the sand mould, chills, i.e., supporting steel bars, and surroundings.

3.3. Residual Stress Analysis

The entire manufacturing process and removal of external loads, i.e., removal of junk material from the NCW, introduces and alters RSs in cast components. Thus, RS evaluation and determination have been studied through laboratory work. Whereas in-depth research performed to calculate their extent and distribution in cast components is limited, especially in the as-cast conditions of HCWCI alloys, which involved solidification and cooling as part of the casting process. After casting processes, i.e., pouring, solidification and cooling, shakeout, and knockout processes, respectively, have been performed, RS measurements were performed in as-cast state in two different manufacturing paths, *viz.*, GCW and NCW states. It is well known that RSs are introduced because of the geometrical complexity of the cast part/component. However, a limited number of works by

 doi:10.20944/preprints202505.0918.v1

scholars and researchers have dealt with the RS's establishment through casting processes, such as casting shakeout at different casting temperatures. Although these RSs are minimum in size, they can still initiate crack establishment. Thus, subsequent failure in later stages of the component during material application and/or service.

Additionally, different stress regions, i.e., P1 and P2 on experimental castings as shown in Figure 2 illustrating GCW [Figure 2a] and NCW [Figure 2b], respectively, in as-cast conditions were measured for RS extent and distribution. Thus, Figures 2–14 demonstrate RS measurements computed from the HDM-RS measurements. Thus, Figs. (A) illustrate principal stresses, i.e., minimum ($\sigma_{min.}$) and maximum ($\sigma_{max.}$), which are shown as green and red in colour, respectively. Figs. (B) illustrate Tresca and Von Mises RSs, which are shown as solid and dashed lines, respectively. Responses of surface strains, thus RS in longitudinal and lateral directions corresponding to $\sigma_{min.}$ and $\sigma_{max.}$ principal stresses, were first evaluated to substantiate the viability of the *in-situ* establishment. Definite relations of principal stresses as a function of casting surface depth (CSD), i.e., z (mm), are illustrated in Figs. (A) and (B).

3.3.1. Sample-A (S/A Alloy)

Residual Stresses at P1 of GCW and NCW in S/A

Figure 3 below presents the RS extent and distribution measured on S/A casting at P1 on GCW and NCW, respectively. RS measurements were performed up to a CSD of approximately 0.8mm. It is noticed in Figure 3 that compressive and tensile RS states are experienced on GCW and NCW. It is noted in Figure 3(A) that RS measurements on NCW and GCW only managed to reach a CSD of approximately 0.275 and 0.875mm, respectively. The principal stresses, i.e., $\sigma_{min.}$ and σ_{max} on GCW and NCW near the surface, were measured and found to be approximately -313 and -147MPa, -30 and 150MPa, respectively, at a CSD of approximately 0.04mm. In addition, RSs on NCW increase linearly in tensile state, reaching maximum magnitudes of approximately 241 and 203MPa for $\sigma_{min.}$ and $\sigma_{max.}$, respectively, at CSD of approximately 0.125mm. The GCW compressive stress decreases under a compression state, reaching maximum magnitudes of $\sigma_{min.}$ and $\sigma_{max.}$ principal stresses of approximately 0.4 and 51MPa, respectively, at a CSD of approximately 0.24mm.

While both GCW and NCW RS distributions after reaching maximum magnitudes at 0.24 and 0.15mm CSD, respectively, show a sharp and slight drop in magnitudes reaching a completely compressive state at approximately 0.875 and 0.275mm, respectively. NCW and GCW RS states at maximum CSD, i.e., 0.275 and 0.800mm were calculated at approximately -474 and -113MPa, -150 and -100MPa, respectively, for principal stresses, i.e., $\sigma_{min.}$ and σ_{max}. The existing RS state and distribution as shown in Figure 3(A) are revealing that there is RS relaxation through casting springing back to its original stress state on NCW after removal of junk material. Thus, it alters the stress state and distribution to a different stress state and distribution on NCW.

Removal of junk material from GCW reveals a completely different RS state and distribution on NCW as shown in Figure 3(A). RSs were established on GCW due to casting processes, such as solidification and cooling, and casting shakeout at approximately 60^{o}C. Therefore, the RS state and distribution are completely relieved and changed to a different stress state and distribution on NCW compared to the RS stress state and distribution on GCW, as presented in Figure 3(A). Figure 3(A) shows that S/A casting component shakeout at 60^{o}C reveals a noticeable consequence on GCW and NCW on the mode the casting component distorts while cooling to ambient temperatures and after removal of junk material from the NCW. This is due to the large temperature gradient that exists at the beginning of the cooling process. However, large temperature gradients gradually lessen as the thermal equilibrium is recognised [22], encouraging tensile stresses on the surface and compressive stresses in the core. Thus, tensile RS increases linearly with increasing CSD as observed in Figure 3(A).

 doi:10.20944/preprints202505.0918.v1

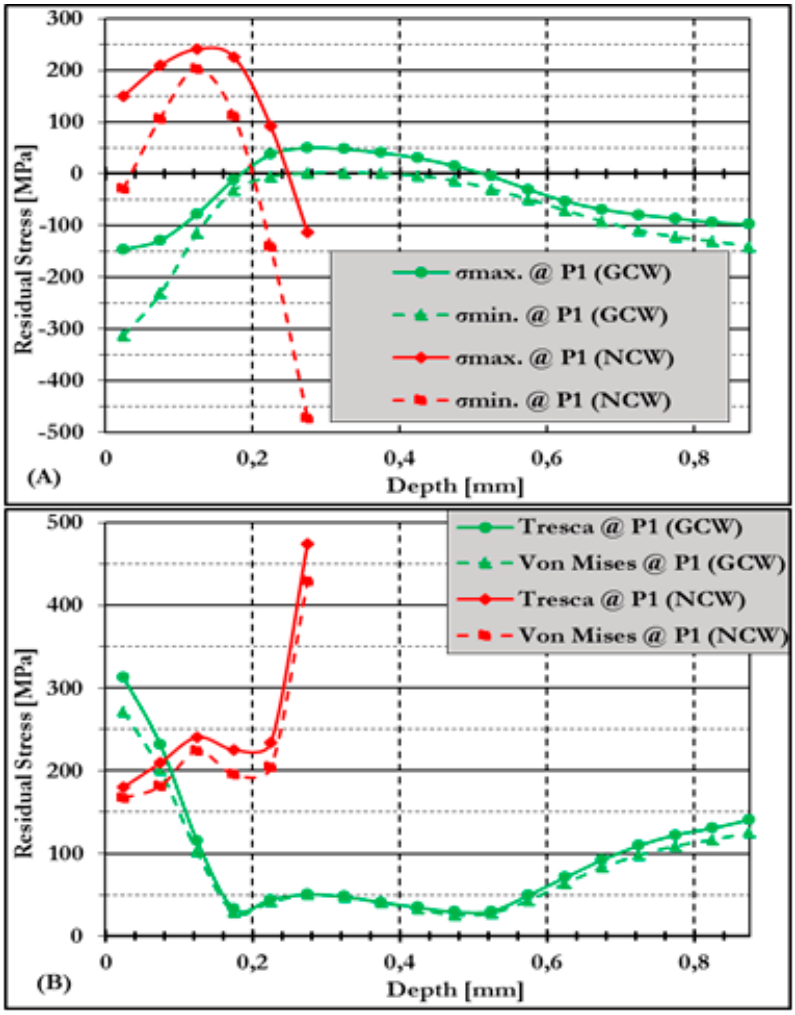

Figure 3. (**A**) Assessment of equivalent RS on NCW versus (vs.) GCW and (**B**) corresponding Von Mises vs. Tresca stresses at P1.

Furthermore, it is observed in Figure 3(B) that RS magnitudes are higher near casting surfaces, i.e., at approximately 0.025mm on GCW with Von Mises and Tresca RS magnitudes of approximately 271 and 313MPa, respectively. While NCW Von Mises and Tresca RSs were measured at approximately 167 and 180MPa, respectively. It is noted that as the CSD increases linearly, there is a linear increase of an equivalent stress on both NCW and GCW. Equivalent Von Mises and Tresca RSs on GCW shown in Figure 3(B) are reducing linearly, reaching minimum levels of approximately 29 and 33MPa at CSD of 0.175mm. While 224 and 241MPa at CSD of approximately 0.125mm on NCW casting components, of equivalent Von Mises and Tresca RSs, respectively, were measured. Equivalent Von Mises and Tresca RSs are to an extent levelling and rising, reaching maximum magnitudes of approximately 125 and 141MPa, respectively, at CSD of approximately 0.875mm. Finally, 195 and 226MPa at CSD of approximately 0.175mm, there is an insignificant rise to maximum magnitudes of approximately 429 and 474MPa at CSD of 0.275mm of equivalent Von Mises and Tresca RSs, respectively.

It is noticed in Figure 3(B) that equivalent Von Mises and Tresca RSs obtained have higher magnitudes near casting surfaces on GCW and at casting interiors on NCW. While Ammar & Shirinzadeh [31] cited that at maximum temperatures, casting components yield effortlessly, such that thermal strains lead to plastic deformation. Nevertheless, during the cooling casting component, the casting no longer yields; thus, thermal strains result in appearing as elastic RSs. It can be concluded that in as-cast conditions, the casting RSs are kept or deposited on the casting component due to solidification and cooling processes, coupled with a temperature gradient, plus a casting

 doi:10.20944/preprints202505.0918.v1

shakeout process performed at approximately 60°C. A substantial large amount of RS magnitude within the casting component in as-cast conditions is stored once the casting component has cooled sufficiently. Any minimum applied stress in magnitude as compared to attained flow stresses establishes an elastic strain, and the plastic strains are not calmed by plastic deformation when the junk materials are removed, leading to the casting component springing back to its original stress state [24,64]. Thus, it is noticed that RSs are inhomogeneous, as noticed in Figure 3 [7,9,24,65]. Additionally, the distribution of RSs with cross-sectional area is inhomogeneous, as illustrated in Figure 3 [7,9,65].

Residual Stresses at P2 of GCW and NCW in S/A

A comparison of NCW and GCW stress states is shown in Figure 4 below at P2 in as-cast conditions. Figure 4(A) shows that GCW and NCW principal stresses, i.e., $\sigma_{min.}$ and $\sigma_{max.}$, near the surface are approximately 133 and 407MPa, 427 and 538MPa at CSD of approximately 0.025 and 0.012mm, respectively. Thus, the magnitudes of RSs of NCW near the surface are higher than those of GCW at P2. It is observed in Figure 4(A) that as the surface depth increases on NCW, the RS principal stresses, i.e., $\sigma_{min.}$ and $\sigma_{max.}$, rise to maximum magnitudes of approximately 624 and 958MPa at the CSD of 0.062 and 0.087mm, respectively. The GCW increases in compression stresses, attaining completely compressive stresses of approximately -180 and -158MPa at the CSD of approximately 0.125mm. It is noted that the drilling process only managed to drill up to a surface depth of approximately 0.125mm on NCW as compared to GCW, i.e., 0.875mm.

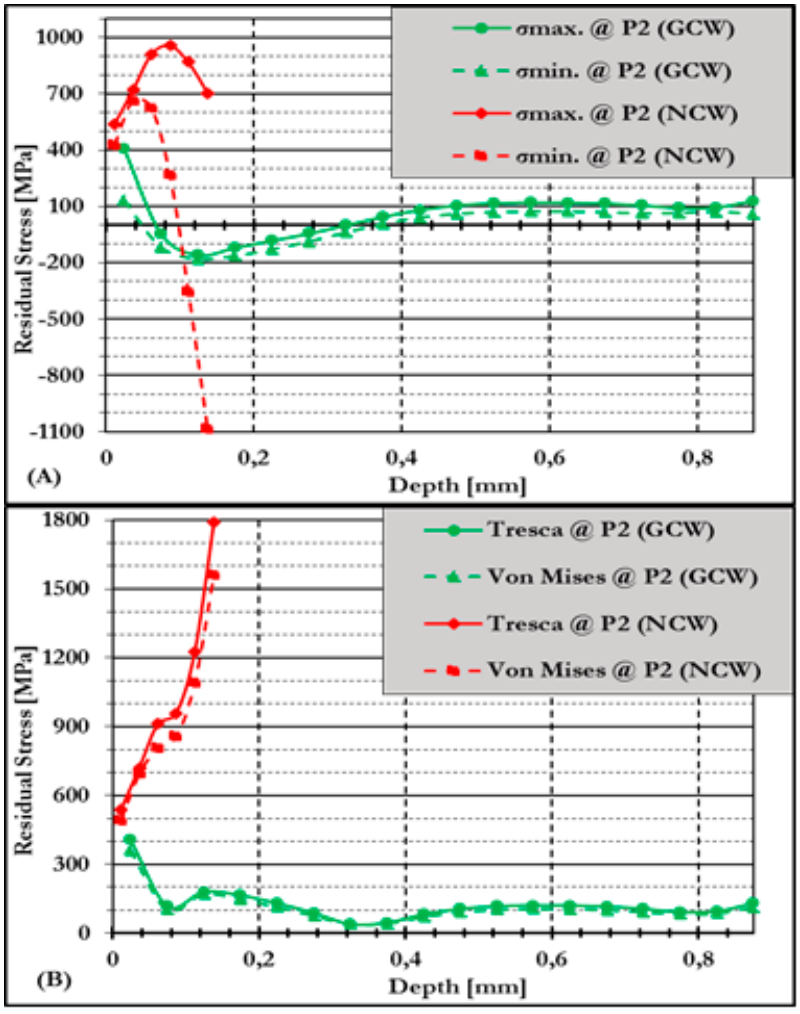

Figure 4. (**A**) Assessment of equivalent RS on NCW vs. GCW and (**B**) corresponding Von Mises vs. Tresca stresses at P2.

 doi:10.20944/preprints202505.0918.v1

Furthermore, GCW RS after attaining completely compressive stresses, it increases slightly in tensile stresses and stays stable with RS magnitudes of approximately 100MPa until it reaches a maximum CSD of approximately 0.875mm. Thus, NCW RS are higher than GCW RS. Figure 4(B) evaluates NCW and GCW RSs on equivalent and computed Von Mises and Tresca RSs. Figure 4(B) reveals that Von Mises and Tresca RSs on NCW are at maximum magnitude as compared to GCW. Equivalent and computed Von Mises and Tresca RSs are at maximum near the casting surface and in inner layers, with computed Von Mises and Tresca RSs reaching 492 and 538MPa at CSD of approximately 0.012mm on NCW. Whereas computed RSs of equivalent Von Mises and Tresca are approximately 359 and 407MPa at CSD of approximately 0.025mm, respectively.

Furthermore, NCW and GCW RSs are lessening linearly with the rise of CSD reaching fully compressive and tensile stresses, respectively, as noticed in Figure 4(B). It is noticed that there is an increase of equivalent computed stresses, i.e., Von Mises and Tresca, as the CSD increases, reaching approximately 1563 and 1790MPa at 0.138mm on NCW. While on GCW, measured and computed equivalent stresses of Von Mises and Tresca RSs, respectively, are approximately 170 and 180MPa at CSD of approximately 0.125mm. Finally, equivalent RSs on GCW remain and endure to an extent of levelling up to a maximum CSD reaching equivalent RSs of ≤ 200MPa. Thus, loading and unloading of junk material effects are observed and found near the casting surface within the casting's various section thicknesses and/or areas, such as at P1 and P2, where RSs are established due to the solidification and cooling process coupled with shakeout at lower casting temperatures, i.e., 60^{o}C in an as-cast condition on GCW.

Residual Stresses on GCW at P1 and P2 in S/A

It is critical to note the differences in the stress strain versus temperature relationship, which is fundamentally important to the establishment of casting RSs [7,22]. During casting processes, solidification, and cooling rate variations, i.e., temperature gradients, are the principal foundation of RSs within casting components, which are due to variations in casting section thickness as highlighted. Thus, Figure 5 below presents the relationship at P1 and P2 on GCW RS measurements. As shown in Figure 5(A), higher RS magnitudes, i.e., principal stresses, such as $\sigma_{min.}$ and $\sigma_{max.}$, are observed at P2 as compared to P1. Near the surface, i.e., 0.025mm CSD at P2 principal stresses, i.e., $\sigma_{min.}$ and $\sigma_{max.}$, are observed to be approximately 133 and 407MPa, whereas at P1, RSs were measured to be approximately -313 and -147MPa. Thus, near the surface, RSs are in a tension state at P2 as compared to P1, which is in a compression state on GCW.

Figure 5(A) reveals that as the CSD increases, P1 and P2 RSs on GCW are completely different near the casting surface, whereas in the surface they are completely different since they fluctuate between tensile and compressive states as observed in Figure 5(A). Since P1 RSs are in a compression state near the casting surface, tensile stresses are increasing as the CSD increases, attaining principal stresses, i.e., $\sigma_{min.}$ and $\sigma_{max.}$ of approximately 74 and 121MPa at a CSD of approximately 0.575mm. Whereas at P2 RSs, increases in compressive stresses as the CSD, i.e., 0.125mm, increase, attaining a completely compressed state of approximately -180 and -158MPa of principal stresses, i.e., $\sigma_{min.}$ and $\sigma_{max.}$, respectively. It is noticed in Figure 5(A) that at P1 and P2, RSs change as the surface depth increases, reaching fully compressive and tension states, respectively. Principal stresses, i.e., $\sigma_{min.}$ and $\sigma_{max.}$, at P1 were measured to be approximately -141 and -98MPa at CSD of approximately 0.875mm, which are fully compressive, whereas at P2 the measured RSs were approximately 61 and 130MPa, respectively. Since P1 is in tensile stresses near the casting surface, whereas P2 is completely in a compression state. It can be concluded that P1 is having thicker section thickness, and it is closer to the feeder/riser, thus experiencing higher magnitudes of tensile stresses as shown in Figure 5(A) near the casting surface.

 doi:10.20944/preprints202505.0918.v1

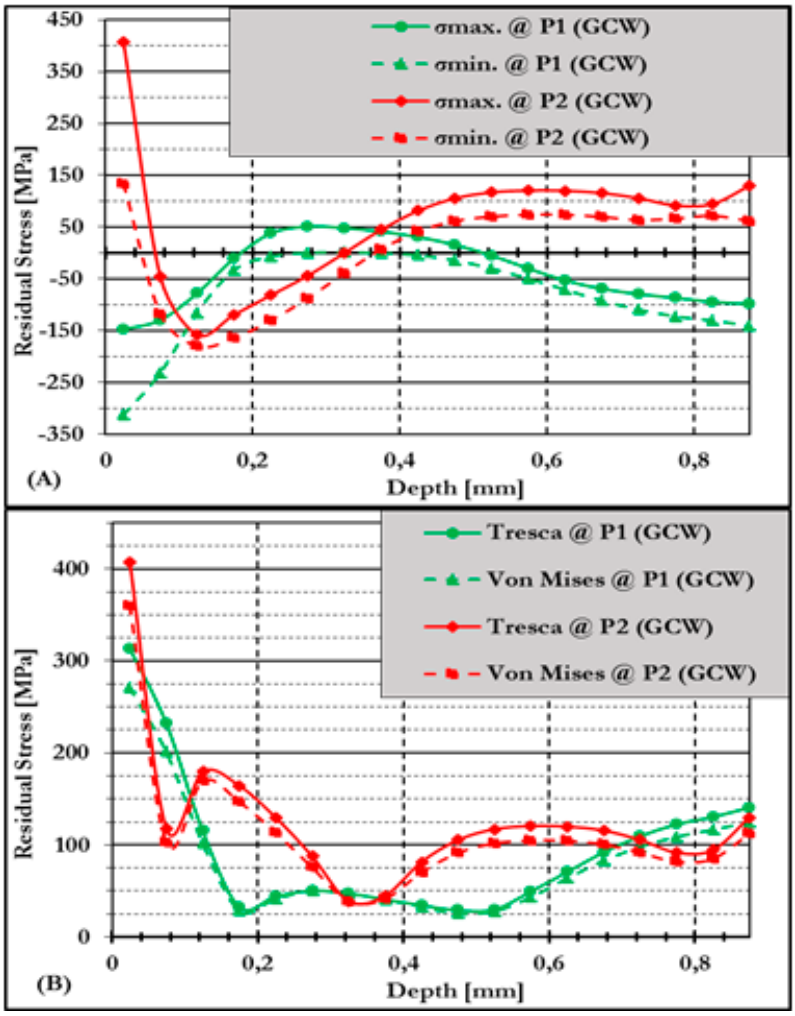

Figure 5. (**A**) Assessment of RS at P1 and P2, and (**B**) Von Mises vs. Tresca stresses within GCW.

Thus, Torres et al. [24] established that thick casting section members normally encourage high tensile stress, hence bending leading to distortions to develop. Corresponding Von Mises and Tresca RSs are illustrated in Figure 5(B) and are noticed to be optimum near casting surfaces at P2 and are computed at approximately 359 and 407MPa, whereas at P1 they are computed at approximately 271 and 313MPa at CSD of approximately 0.025mm, respectively. Additionally, at a CSD of approximately 0.075mm, corresponding Von Mises and Tresca RSs are lessening as the CSD rises, reaching 201 and 232MPa, 103 and 117MPa at P1 and P2, respectively. While computed Von Mises and Tresca RSs at P1 remain to decline linearly, reaching approximately 29 and 33MPa at CSD of approximately 0.175mm, respectively.

Furthermore, at P2, Von Mises and Tresca RSs are reduced significantly and show levels of variation, thus reaching computed Von Mises and Tresca RSs of approximately 39MPa at approximately CSD of 0.325mm for both RSs and 112 and 130MPa at CSD of approximately 0.875mm. Computed RSs of Von Mises and Tresca at P1 rise linearly with increasing CSD, reaching 50 and 51MPa at approximately 0.275mm CSD. As well, Von Mises and Tresca RSs are lessening to some extent, reaching approximately 28 and 30MPa, respectively, at approximately 0.525mm CSD. Whereas corresponding RSs rise with an increasing CSD, reaching approximately 0.875mm, and Von Mises and Tresca RSs of approximately 125 and 141MPa, respectively. Thus, RSs attained agreement with earlier studies achieved by other scholars and/or researchers.

Throughout the casting processes of special casting design, i.e., complex shapes, the cooling rates of other sections are normally constrained by some regions that may have cooled initially and are much stronger, thus leading to weaker casting sections to plastic deformation. During the casting of

 doi:10.20944/preprints202505.0918.v1

exceptional designs and/or stress lattice casting, i.e., complex shapes, the cooling of some regions is often constrained by other regions that have cooled earlier and thus are stronger, causing the weaker regions to plastic deform [7,24,66]. The phenomena lead to casting components experiencing various stress conditions and/or states as presented in Figure 5(A). Thus, the phenomena result in a casting component experiencing different stress states at different casting regions, as shown in Figure 5(A).

Akhtar [22] and Zhang et al. [63] established that stressed castings are under-cooled from a solidification state; the variations due to cooling rates lead to the establishment of a tensile RS state within inner regions and a compressive RS state in the external areas. In addition, casting components of complex geometry, the external surface, i.e., the casting surface, will show variations and not only have an impact on thermal RSs but also on the microstructural features developed within the final casting component [7,67]. Thus, it can be concluded from the evaluation of RSs obtained in Figure 5 that RS magnitudes of a given casting component can experience RS magnitudes relying on the degree of limitation executed by other casting regions and/or sections through fast cooling of earlier sections than others and the degree of constraints experienced through sand mould walls [7,66].

Residual Stresses on NCW at P1 and P2 in S/A

Since it was noticed that there is deflection and the material is springing back when junk materials are removed from NCW, RSs were compared on NCW at P1 and P2. It is observed in Figure 6(A) below that at P1 and P2 $\sigma_{max.}$ principal stresses are presented in the tensile region. Whereas both compressive and tensile regions on $\sigma_{min.}$ principal stresses were noticed on both P1 and P2 as the surface depth increases. These findings are not in agreement with some scholars' findings; thus, there is an increase in RS as the casting surface depth increases, as observed in Figure 6(A). Near the casting surface, it is noticed that RSs are in slightly compressive and tensile states at P1 with a measured RS of approximately -30 and 150MPa at the CSD of approximately 0.025mm on $\sigma_{min.}$ and $\sigma_{max.}$ principal stresses, respectively. Whereas at P2, $\sigma_{min.}$ and $\sigma_{max.}$ principal stresses were measured at a magnitude of approximately 427 and 538MPa at the CSD of approximately 0.120mm, respectively.

Additionally, P1 and P2 RS increases linearly as the CSD increases, reaching approximately 203 and 241MPa maximum tensile stress states at the surface depth of approximately 0.125mm, respectively, at P1. At a surface depth of approximately 0.037mm, $\sigma_{min.}$ and $\sigma_{max.}$ principal stresses were measured as 665 and 958MPa, respectively, at P2. It is noticed in Figure 6(A) that RSs at P1 are lessening linearly as the CSD increases, reaching a completely compressive stress state of approximately -474 and -113MPa at the CSD of approximately 0.275mm, whereas at P2 RSs are both in compressive and tension stress states of approximately -1085 and 705MPa on $\sigma_{min.}$ and $\sigma_{max.}$ principal stresses, respectively.

Corresponding and computed Von Mises and Tresca RSs at P1 and P2 are revealed in Figure 6(B). It is revealed that computed Von Mises and Tresca RSs magnitude at P2 are optimum as compared to P1. Thus, it is observed that computed Von Mises and Tresca RSs near the casting surface are reaching approximately 167 and 180MPa at CSD of approximately 0.025mm at P1, whereas at P2 they are computed at approximately 492 and 538MPa at CSD of approximately 0.012mm. It is noticed that as the CSD rises, computed RSs, i.e., Von Mises and Tresca at P2, are rising linearly, reaching 1562 and 1790MPa at a CSD of approximately 0.138mm. Whereas RSs at P1, computed Von Mises and Tresca RSs are to some extent rises reaching 204 and 234MPa at CSD of approximately 0.225mm, thus attaining optimum RSs of approximately 429 and 474MPa at CSD of approximately 0.275mm, respectively.

 doi:10.20944/preprints202505.0918.v1

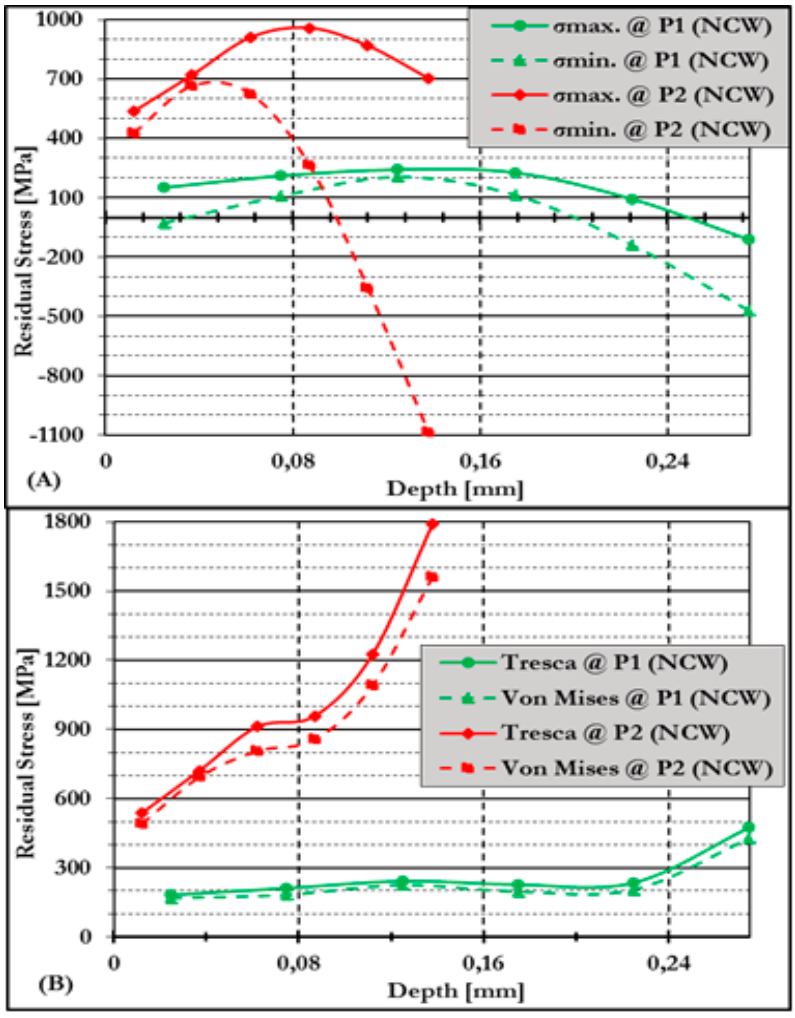

Figure 6. (**A**) Assessment of RS at P1 and P2, and (**B**) corresponding Von Mises vs. Tresca stresses within NCW.

As shown in Figure 5, established RSs are revealing optimum magnitudes within GCW at P2 as compared to P1. Whereas Figure 6 corresponds and/or matches RSs established in Figure 5 and P2 RSs on NCW are revealing optimum magnitudes as compared to P1. Uneven cooling leads to distortions of cast components/parts due to casting variation section thickness cooling differently, i.e., variation in cooling rates, thus relying on the volume-to-surface ratio, i.e., casting modulus and thermal conductivity of the sand mould in contact with the casting component, the design of the cooling lines within the sand mould, which affects the path heat is extracted from the cast component, i.e., iron, and the presence of the core/s [66]. Therefore, all these parameters and/or factors establish and can be used to determine the RSs magnitudes and/or RSs are more difficult to project, as can be observed in Figure 6.

3.3.2. Sample-B (S/B Alloy)

Residual Stresses at P1 of GCW and NCW in S/B

RSs on GCW and NCW at P1 are compared as presented in Figure 7 below. Extremely higher tensile stress states are noticed on GCW, especially within the inner layers, i.e., at approximately between CSD of approximately 0.2 and 0.6mm as observed in Figure 7(A). Whereas near casting surfaces on GCW, RS to some extent are highly in a compressive stress state. In addition, a compressive steady RS state on NCW is noticed as compared to GCW. It is noticed that the compressive steady stress state is through the casting surface, i.e., from casting surfaces through the inner layers of the casting component. It is concluded that RSs on NCW are completely relieved after

 doi:10.20944/preprints202505.0918.v1

removal of junk material from the NCW. This is due to the extremely high tensile RS state observed on GCW as compared to the RS on the NCW casting component observed in Figure 7(A). RS states within NCW are altered, i.e., tensile stress to compressive stress state due to the removal of junk material from the NCW, leading to a completely different RS state and distribution. Since RSs has been induced due to a large temperature gradient, which is from the casting surface "*external layer*" to the inner layers "*centre*," depending on the casting dimensions, i.e., the sections thickness of the casting, RSs could be related to the comprehensive rate of cooling. Thus, attainment of substantial proportions under rapid cooling will lead to RSs, which is due to casting shakeout at approximately 180^{o}C.

Furthermore, structural and compositional heterogeneity will add to the cause of RSs development. Mould hindrance and phase transformations contribute appreciable quantities of RSs when higher magnitudes of temperature gradient exist among casting sections of the casting during cooling [7,22,68]. The action of contraction of the casting causes a build-up of RSs at the latter stages of cooling. Thus, considering that the material will not develop RSs while in the liquid state, i.e., in the interior "*centre*" of the casting, but RSs will arise as the solidification progresses beyond the eutectic reaction, i.e., for an alloy. Figure 7(A) shows that near the casting surface on GCW, principal stresses, i.e., $\sigma_{min.}$ and $\sigma_{max.}$, respectively, are in a completely compressive stress state, whereas on NCW they are between a slightly tensile and a completely compressive steady stress state. It is noticed in Figure 7(A) that $\sigma_{min.}$ and $\sigma_{max.}$ principal stresses are measured near the casting surface at approximately -103 and0 -48MPa at approximately 0.04mm, respectively, on GCW. Whereas $\sigma_{min.}$ and $\sigma_{max.}$ principal stresses on NCW are approximately -215 and 163MPa at approximately 0.025mm, respectively.

Furthermore, steady compressive RSs are noticed on NCW to have been established with measured RSs within maximum magnitudes of approximately -250MPa till CSD is at maximum, with an extent of approximately -20 and 53MPa at approximately 0.875mm measured for tensile and compressive stresses, respectively. It is noticed that GCW RSs are lessening linearly as the CSD rises and reaches RSs of approximately -490 and -241MPa at CSD of approximately 0.68mm, while to some extent it lessens slightly within compressive RSs reaching approximately -214 and -86MPa at CSD of approximately 0.875mm, respectively.

However, Figure 7(B) reveals that near CSD of up to a maximum of approximately 0.2mm on NCW, Von Mises and Tresca RSs are at optimum as compared to GCW. Whereas at CSDs of approximately 0.025 and 0.04mm, Von Mises and Tresca RSs within NCW and GCW are measured at approximately 328 and 378MPa, 89 and 103MPa, respectively. The corresponding RSs shown in Figure 7(B) illustrate that within NCW, computed RSs of Von Mises and Tresca are lessening and are approximately measured below 200MPa util they reach a CSD of approximately 0.875mm. Whereas on GCW, computed RSs of Von Mises and Tresca are computed at approximately 1101 and 1122MPA at CSD of approximately 0.44mm, respectively. Computed RSs as shown in Figure 7(B), GCWs are lessening with rising CSD reaching 199 and 212MPA at approximately 0.60mm, and rises reaching 426 and 490MPa at approximately 0.68mm CSD within computed Von Mises and Tresca RSs, respectively.

Finally, computed RSs within GCW, Von Mises, and Tresca RSs are lessening and measured at approximately 61 and 64MPa at CSD of approximately 0.92mm, respectively. Shakeout processes at higher casting temperatures are noticed to establish optimum magnitudes of tensile stresses within the cores of the casting at P1 on GCW. While tensile stresses on GCW are relieved and fully steady-state and/or compressive RSs of lower magnitude are established within NCW, as shown in Figure 7(B).

 doi:10.20944/preprints202505.0918.v1

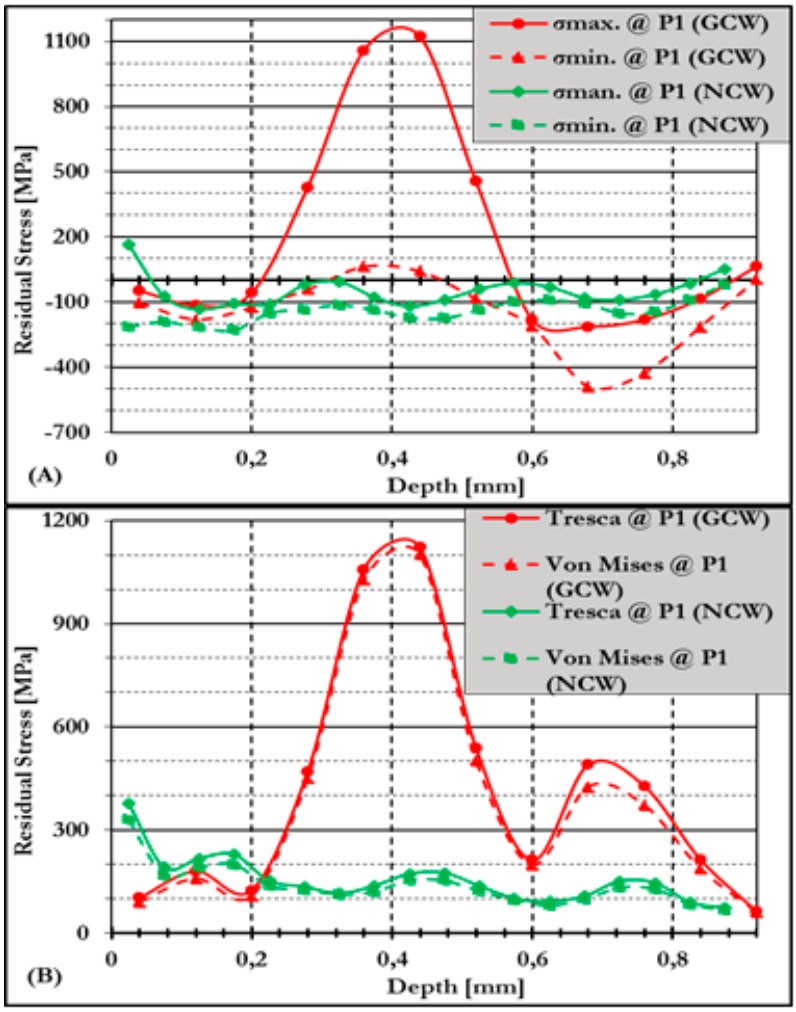

Figure 7. (**A**) Assessment of equivalent RS on NCW vs. GCW and (**B**) corresponding Von Mises vs. Tresca stresses at P1.

Residual Stresses at P2 of GCW and NCW in S/B

Since junk material has been removed from NWC, Figure 8 below illustrates RSs on GCW and NCW at P2 in as-cast conditions. Highly compressive stresses can be observed on GCW as compared to NCW. Whereas NCW shows that RSs in a compressive state are lessening due to the removal of junk material from the NCW, as observed in Figure 8(A). It is noticed that the RSs observed on NCW are steady with slight fluctuations. Thus, elastic relaxation is due to junk material removed from the GCW, which proves that after removal of the gating system, i.e., runners from GCW, the material springs back to its original state.

Figure 8(A) shows that GCW principal stresses, i.e., $\sigma_{min.}$ and $\sigma_{max.}$, are to some extent in a compression and tension state of approximately -20 and 130MPa, respectively, at a CSD of approximately 0.01mm. Whereas NCW principal stresses, i.e., $\sigma_{min.}$ and $\sigma_{max.}$, are 2 and 30MPa, respectively, at a CSD of approximately 0.013mm and increase in compression state linearly as the casting depth increases, achieving a determined compressive stress state of approximately -611 and -241MPa of CSD a of approximately 0.33mm on GCW, as observed in Figure 8(A). Points of fluctuations start to show on GCW as the CSD increases, reaching principal stresses flanked at CSD between 0.59 and 0.87mm, observing RSs magnitudes of approximately 6 and 23MPa, 6 and 23MPa, respectively, on $\sigma_{max.}$ principal stresses. Whereas -22 and -95MPa at CSD of approximately 0.87mm on $\sigma_{min.}$ principal stresses. Thus, the increase in RSs is linear in a compressive state and continued to be steady at compressive regions below measured RS values of approximately -180MPa.

 doi:10.20944/preprints202505.0918.v1

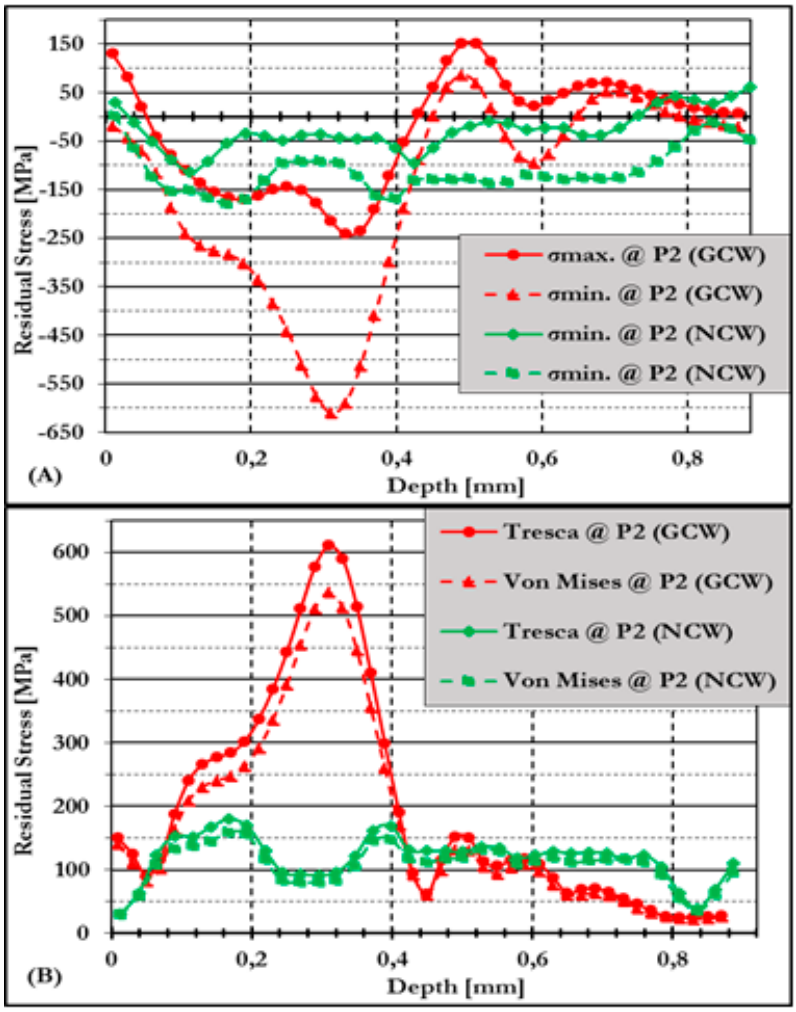

Figure 8. (**A**) Assessment of equivalent RS on NCW vs. GCW and (**B**) corresponding Von Mises vs. Tresca stresses at P2.

Corresponding Von Mises and Tresca RSs shown in Figure 8(B) are noticed to be optimum near the casting surface on GCW with computed RSs measured at approximately 140 and 149MPa, respectively, at a CSD of approximately 0.01mm. Whereas on NCW, corresponding RSs of Von Mises and Tresca are approximately 29 and 30MPa, respectively, at a CSD of approximately 0.013mm. Furthermore, corresponding RSs of Von Mises and Tresca are rising linearly as the CSD increases and computed at approximately 536 and 611MPa, respectively, at a CSD of approximately 0.31mm on GCW. Whereas at NCW, corresponding Von Mises and Tresca RSs are to some extent established to rise slightly and are computed at approximately 159 and 180MPa, respectively, at a CSD of approximately 0.167mm.

It is further noticed that corresponding RSs on GCW are lessening linearly with increasing casting surface, and Von Mises and Tresca are measured at approximately 170 and 190MPa at approximately 0.41mm CSD. Whereas on NCW, corresponding Von Mises and Tresca RSs are showing variations and start to be stable beneath 69MPa. Finally, GCW both corresponding Von Mises and Tresca RSs rise and lessen as the casting surface increases, reaching 61MPa at approximately 0.45mm CSD. Corresponding Von Mises and Tresca RSs rise and lessen to some extent as the casting surface increases, reaching 25 and 30MPa, 132 and 151MPa at CSD of approximately 0.87mm, respectively. Therefore, corresponding Von Mises and Tresca RSs are fully relieved during the removal of junk material from the NCW, as revealed in Figure 8(B) within P1 and P2, respectively. While it is established that RS magnitudes established within the S/B casting component present a series of experiments that are greater and stable, respectively.

 doi:10.20944/preprints202505.0918.v1

Residual Stresses on GCW at P1 and P2 in S/B

It is observed that Figure 9 below illustrates RS measurements at P1 and P2 on GCW in as-cast conditions. While it is noted that during solidification and cooling processes, temperature gradients are established due to various casting section thicknesses, thus leading to variances in the rate of contraction on various casting sections within casting components while consequential RSs are generated within casting components, especially on GCW. Usually, temperature variances are due to dissimilarities in casting size within cross-sectional areas and due to the distance of the liquid metal from the heads and gates [7,14]. During solidification and cooling processes, there exist temperature differences and are the chief source of RS formation on casting components.

Thus, an attempt to lessen the temperature differences within casting during solidification and cooling will lead to lessening of RS [7,14,24]. When casting components are separated and removed from sand moulds, i.e., casting shakeout processes, casting strains rise due to high Cr-iron having imperfect and/or limited yield points and limited ductility. However, minor plastic strains at all stress levels are experienced on casting components. Thus, the strains signify plastic and elastic deformation [7,14]. The RSs shown in Figure 9(A) are illustrations of RSs and distributions that are noticed to be optimum near casting surfaces at P2 compared to P1. In addition, tensile stresses are noticed to be within P1, while P2 illustrates minimal compressive RSs. Therefore, at a CSD of approximately 0.6mm until optimum CSD, RSs are noticed to be in a tensile state at P2, while at P1 they are in a compressive stress state.

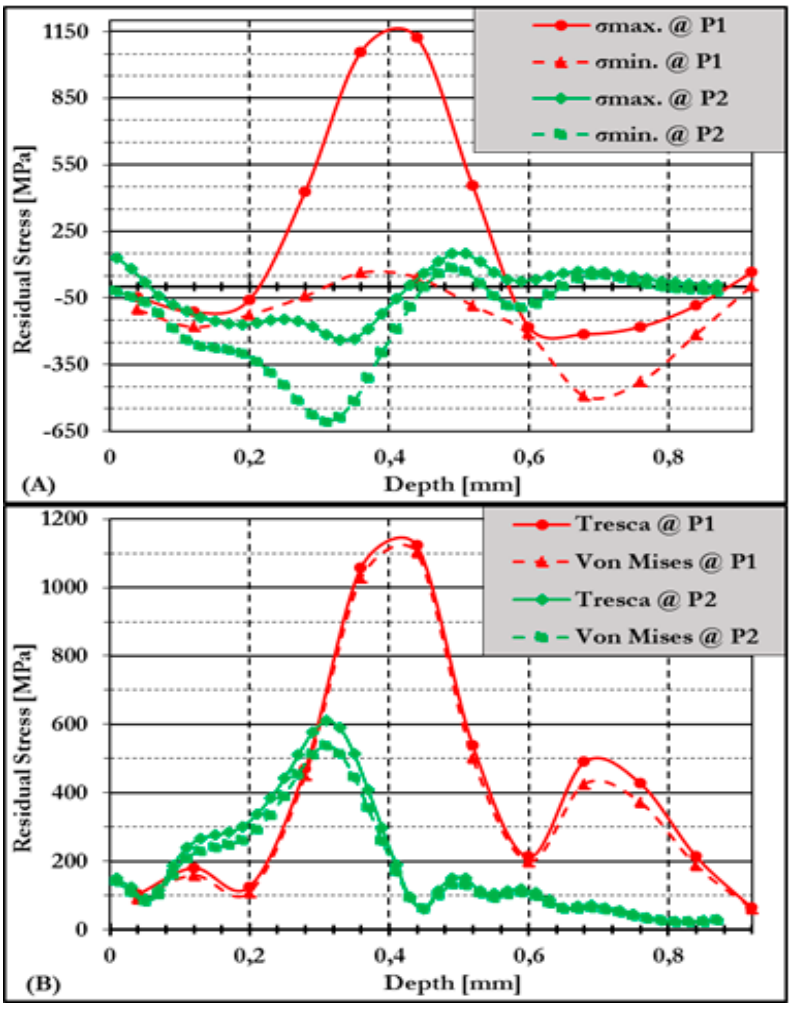

Figure 9. (**A**) Assessment of RS at P1 and P2, and (**B**) corresponding Von Mises vs. Tresca stresses within GCW at P2.

 doi:10.20944/preprints202505.0918.v1

Furthermore, Figure 9(B) reveals computed RSs of Von Mises and Tresca, which reveal optimum magnitudes near casting surfaces, i.e., 0.29mm within P2, while P1 reveals optimum RSs after 0.29mm till it reaches optimum CSD. Computed RSs of Von Mises and Tresca as presented in Figure 9(B) are approximately 140 and 149MPa at CSD of 0.01mm, while both computed RSs rise linearly, reaching 1102 and 1122MPa at P1 and at CSD of approximately 0.44mm, respectively. It is noticed that P2 computed Von Mises and Tresca RSs reaches 511 and 577MPa, respectively, at a CSD of 0.29mm. In addition, computed Von Mises and Tresca stresses are lessening linearly with rising CSD, reaching 199 and 212MPa at CSD of approximately 0.60mm within P1, while within P2 reaches similar RS distribution of approximately 61MPa at CSD of approximately 0.45mm.

Computed Von Mises and Tresca RSs rise as the CSD increases, reaching 426 and 490MPa at a CSD of approximately 0.68mm, and lessening, reaching minimal magnitudes at a CSD of approximately 0.92mm with computed magnitudes of approximately 61 and 64MPa within P1. While P2 rises to some extent and lessens reaching minimal magnitudes of approximately 25 and 28MPa of computed RSs of Von Mises and Tresca, respectively, at CSD of approximately 087mm. Since it is noticed that near-casting surface RSs are optimum within P1, while within inner casting surfaces at P2 are optimum. Therefore, it is concluded that the obtained results during shakeout processes of high Cr-irons at optimum temperatures establish optimum magnitudes of tensile stresses within P1 as compared to P2 with compressive stress states. Akhtar [22] cited that air cooling introduces extensive added RS, while [69] cited that casting modules show a significant part in RS matter and that RS rises as ductility lessens.

Residual Stresses on NCW at P1 and P2 in S/B

Alipooramirabad et al. [25] in their studies cited that the transformation among casting section thicknesses, i.e., P1 and P2 RS state and distribution curves, is established from variations in size and weight of various casting sections, which have an impact on the solidification and cooling rates, thus variations in thermal gradients. Thus, Figure 10 below reveals equivalent principal stresses computed, leading to Von Mises and Tresca RSs magnitudes between P1 and P2 on NCW in as-cast conditions. Whereas Figure 10(A) illustrates principal stresses, i.e., $\sigma_{min.}$ and $\sigma_{max.}$ at P1 measured at approximately 215 and 163MPa at CSD of approximately 0.025mm and at P2 RSs measured at approximately 2 and 3MPa at CSD approximately 0.013mm, respectively. Additionally, $\sigma_{min.}$ and $\sigma_{max.}$ principal stresses lessen linearly with rising CSD, reaching an optimum of approximately -152 and -134MPa at CSD of approximately 0.225mm at P1. Additionally, $\sigma_{min.}$ and $\sigma_{max.}$ principal stresses at P2 RSs attain an optimum RS of approximately -180MPa (0.116mm) and -114MPa (0.167mm).

While P1 and P2 principal stresses start to reveal elevated levels of instability with an increasing CSD. At CSD of 0.2 to 0.887mm at P1, $\sigma_{min.}$ and $\sigma_{max.}$ principal stresses start to show variations of RSs of approximately -175 and -7MPa, respectively. Principal stresses, such as $\sigma_{min.}$ and $\sigma_{max.}$ at P2, show levels of variation between -169 and 42MPa. Thus, it can be concluded that NCW RSs are relieved and/or relaxed, since computed stresses are revealing stability in the compressive region as shown in Figure 10(A). It is noticed near the casting surface, i.e., at CSD of approximately 0.025 and 0.013mm as shown in Figure 10(B), that computed RSs of Von Mises and Tresca are approximately 328 and 378MPa at P1, while at P2 they are computed at 29 and 30MPa, respectively. In addition, at P1, computed Von Mises and Tresca RSs are lessening linearly with increasing CSD, reaching RSs of approximately 199 and 229MPa at approximately 0.175mm, respectively. While at P2, computed Von Mises and Tresca RSs rise as the CSD rises, reaching 159 and 180MPa at approximately 0.167mm, respectively. Figure 10(B) reveals that corresponding Von Mises and Tresca RSs are lessening linearly and start to show variations with increasing CSD at P1, whereas at P2 to some extent reveal slight variations and become stable and lessening and rise slightly.

 doi:10.20944/preprints202505.0918.v1

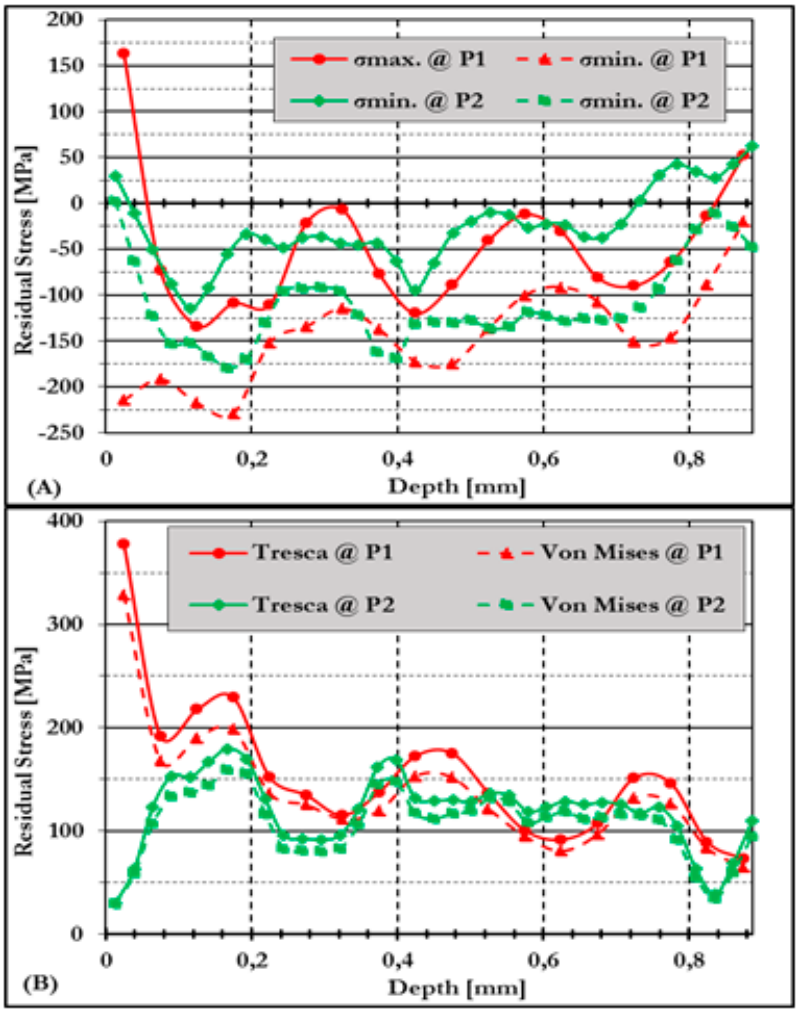

Figure 10. (**A**) Assessment of RS at P1 and P2, and (**B**) corresponding Von Mises vs. Tresca stresses within NCW.

Thus, it can be concluded that at P1, computed RSs attain optimum magnitudes up to CSD of approximately 0.32mm as compared to P2. In addition, at P1, corresponding Von Mises and Tresca RSs are computed to some extent greater and computed between 80 and 172MPa, whereas at P2 they are computed at 111 and 123MPa, respectively. Thus, the degree of RS relaxation and/or relief is neither tough to envisage, and the remaining course of action is to adopt that easing takes place after removal of junk material from NCW. while greater magnitudes of RSs are established at P1 as compared to P2 within NCW in as-cast conditions.

3.3.3. Residual Stresses on S/A and S/B

The distribution of RS in hypoeutectic alloys of HCWCI disturbs mechanical and fatigue properties, respectively. Whereas solidification and cooling conditions, such as time and parameters, i.e., casting shakeout temperature and knockout time, affect the state of RS and can be of great standing, particularly in a manufacturing environment, i.e., the foundry industry, and for product quality. In addition, during casting processes, sand moulds plus cores are additionally a restriction to the deformation and thermal contraction overall. Thus, leading to stress and/or relaxation of the casting component [7,25,70]. During the casting process in the current study, RS are established due to solidification and cooling processes, whereas the knockout of junk material from NCW on GCW adjusts the stress state and RS distribution. Furthermore, casting shakeout at dissimilar temperatures leads to higher RS quantities on hypoeutectic alloys of HCWCI alloys.

 doi:10.20944/preprints202505.0918.v1

Residual Stresses at P1 of GCW on S/A and S/B

S/A and S/B cast component's RS state and distributions attained during RS measurement using incremental HDM on casting components shakeout at lower and higher temperatures, i.e., 60 and 180°C, respectively, are shown in Figure 11 below. Figure 11(A) shows that S/A and S/B cast component's RS states are to some extent in tensile and compressive stress states of approximately -313 and 30MPa, -103 and -48MPa at CSD of approximately 0.025 and 0.04mm, respectively, on $\sigma_{min.}$ and $\sigma_{max.}$ principal stresses. Thus, the S/A and S/B cast component's RS state deviates linearly as the CSD increases towards the casting inner layers. In addition, S/A and S/B cast components principal stresses, i.e., $\sigma_{min.}$ and $\sigma_{max.}$, are showing higher magnitudes of approximately -141 and -65MPa, 43 and 63MPa, respectively, at approximately casting depths between 0.36 and 0.44mm at inner layers. Whereas from a CSD of approximately 0.6mm to maximum surface depth on S/A and S/B cast components, RS states are completely in a compressive state. Thus, the S/A casting component RS is showing lower magnitudes as compared to the S/B casting component RS state.

The higher magnitude of RS is established on the S/B casting component as compared to the S/A casting component due to higher casting shakeout temperatures, i.e., 180°C which are accompanied by fast cooling rates from casting temperatures of approximately 180°C as compared to 60°C. Higher casting shakeout temperatures, i.e., 180°C can be compared to the quenching process, which normally leads to higher RSs, especially tensile stress on the casting surfaces. Hence, higher casting shakeout temperatures are leading to higher temperature gradients from the surface to the core of the casting, coupled with solid contraction. These higher temperature gradients experienced by the casting component lead to higher tensile RSs within the surface and increase as the CSD increases and are lessening as the surface approaches the core of the casting component, thus transforming to a different stress state, i.e., compressive stresses when approaching the centre of the casting component, as can be observed in Figure 11(A).

The magnitude of tensile stresses, which were established at earlier stages of fast cooling, remains within the casting component even at room temperature, thus leading to higher magnitudes of tensile stresses within the surface and steady RS within the core of the casting. Whereas casting shakeout temperatures at lower temperatures, i.e., 60°C and/or at ambient temperatures, are developing a steady state of RSs, which is due to controlled cooling, i.e., reduced cooling rates, thus reducing the temperature gradient in the final stages of cooling, since the casting cools within a sand mould as compared to normal air cooling, i.e., slower cooling rates, which is similar to full annealing thermal processes.

Thus, relieving or reducing the higher RS magnitude of the casting component. S/A and S/B cast products component plastic flow behaviour is observed within computed RSs of Von Mises and Tresca distributions as shown in Figure 11(B). Figure 11(B) illustrates that computed RSs near casting surfaces within S/A cast products are optimum compared to S/B casting components, which are only showing optimum magnitudes within inner surfaces and at optimum CSD. The S/A casting component is noticed to reveal optimum RSs compared to the S/B casting component due to relieved and/or relaxed RSs magnitudes, which is a result of the slow cooling process in the sand mould compared to fast cooling.

In addition, optimum plastic flow has inadequate elastic performance, while minimal plastic performance is accompanied by optimum elastic performance due to the casting component being restrained as a result of the removal of junk material on NCW being relieved and/or relaxed. It is noticed that the corresponding Von Mises and Tresca at the S/A casting component are computed at approximately 271 and 313MPa at approximately 0.025mm near casting surfaces, whereas within the S/B casting component, it is computed at approximately 89 and 103MPa at a CSD of approximately 0.04mm, respectively.

 doi:10.20944/preprints202505.0918.v1

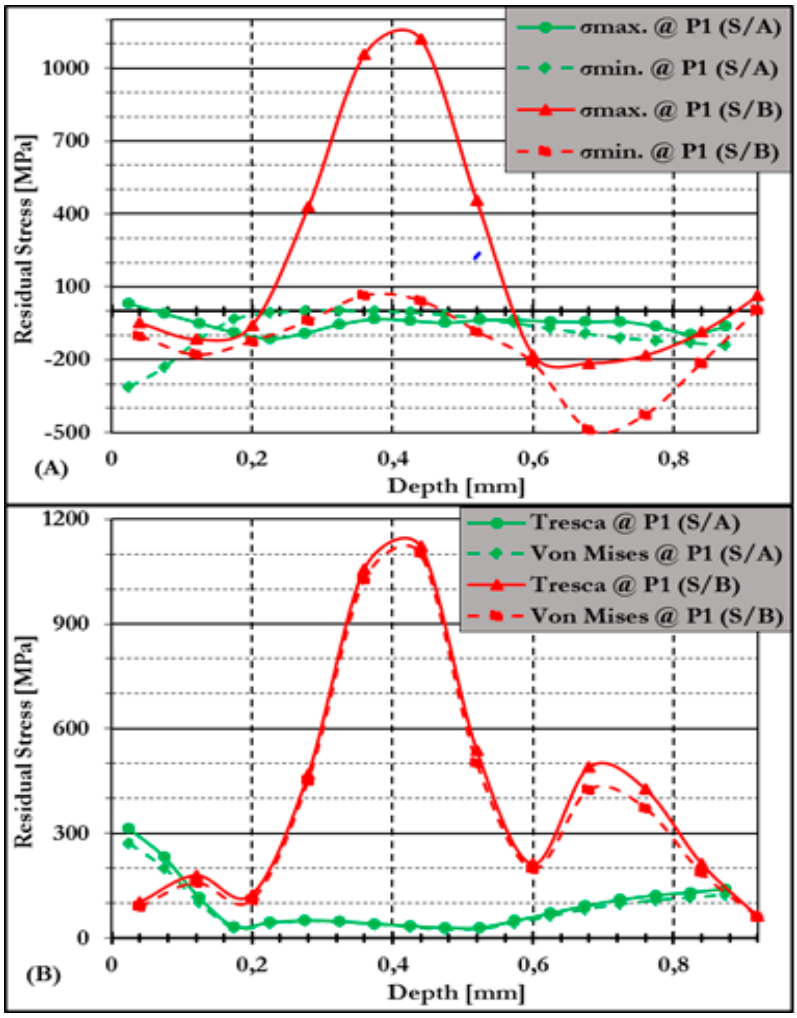

Figure 11. Evaluation regarding S/A vs. S/B-cast products within GCW at P1.

In addition, it is noticed that as the CSD rises, computed RSs of Von Mises and Tresca deviate linearly within S/A and S/B cast products, i.e., cast components with computed stresses of Von Mises and Tresca lessening, thus reaching 29 and 33MPa at CSD of approximately 0.175mm, respectively. Whereas Von Mises and Tresca RSS within the S/B casting component rise and lessen to some extent, reaching 109 and 125MPa at a CSD of approximately 0.2mm, respectively. However, S/A casting component computed Von Mises and Tresca RSs continue to be in a stable state at CSD of approximately 0.875mm between 30 and 33MPa, 125 and 141MPa, respectively. Whereas computed Von Mises and Tresca RSs within the S/B casting component rise linearly with rising CSD, reaching optimum RSs of approximately 1101 and 1058MPa at approximately 0.36 to 0.44mm, respectively. In addition, computed Von Mises and Tresca RSs within the S/B casting component lessened linearly with rising CSD, reaching minimal RSs of approximately 199 and 212MPa at CSDs of approximately 0.60mm, respectively. Finally, S/B casting component Von Mises and Tresca RSs are lessening with rising CSD, reaching minimal RSs of approximately 61 and 64MPa at CSD of approximately 0.90mm, respectively.

From the casting and shakeout processes, respectively, it is concluded that shakeout at optimum temperatures, creep is noticed. Since cooling periods are shortened owing to normal cooling, i.e., air cooling. Additionally, shakeout at approximately 180°C temperatures; time effects lessens owing to rapid cooling rates, thus establishing tensile stress at optimal levels within inner parts within the S/B casting component. Whereas shakeout at minimum temperatures, undeviating cooling rates are noticed owing to sand mould cooling leading to RSs relaxation and/or relief within the S/A casting component as shown in Figure 11. Akhtar [23] and Torres et al. [24] cited in their studies that owing

 doi:10.20944/preprints202505.0918.v1

to established temperature gradients prevailing from casting surfaces to inner surfaces of the casting component due to casting, solidification, and cooling processes, respectively. Ngqase et al. [7] cited that RSs occurring owing to casting, solidification, and cooling processes, respectively, led to reaching appreciable magnitudes. Therefore, it is concluded that maximum casting shakeout temperature established optimum magnitudes of RS within S/A and S/B cast products components with compressive and tensile RSs within GCW.

Residual Stresses at P1 of GCW on S/A and S/B

Comparison of RSs amongst S/A and S/B cast product components at P1 are illustrated in Figure 12 below. It is noticed in Figure 12(A) that RSs in the S/A casting component are completely in a tensile stress state, whereas S/B casting components are completely in a compression stress state, and the evaluation is up to a CSD of approximately 0.275mm. Figure 12(A) shows that near the casting surface, $\sigma_{max.}$ principal stresses amongst S/A and S/B cast product components are totally in a tensile state, while $\sigma_{min.}$ principal stresses are totally in a compressive state. Near the casting surface, principal stresses, i.e., $\sigma_{min.}$ and $\sigma_{max.}$ magnitudes, are restrained on S/A at approximately -30 and 150MPa at CSD of approximately 0.025mm, whereas S/B principal stresses on the casting component are evaluated at approximately -215 and 163MPa, respectively, as noticed in Figure 12(A).

Furthermore, it is noticed that as the casting depth rises, S/A and S/B cast product component RSs are rising linearly, whereas S/A principal stresses are evaluated at approximately 203 and 241MPa at CSD of approximately 0.125mm, and S/B casting component RSs are evaluated reaching maximum magnitudes of approximately -218 and -134MPa on the casting surface of approximately 0.125mm. Thus, $\sigma_{min.}$ and $\sigma_{max.}$ principal stresses are totally in tension and compressive stress states on both S/A and S/B cast product components, respectively. As well as the CSD rises, S/A and S/B RSs are lessening linearly in tensile and in compressive states, respectively. Whereas it is observed and noticed in S/A RSs lessening linearly in tensile stress state, reaching compressive stress state of approximately -474 and -113MPa at CSD of approximately 0.275mm and S/B RSs reaching to some extent compressive stress state of -135 and -21MPa on principal stresses, i.e., $\sigma_{min.}$ and $\sigma_{max.}$, respectively. Finally, S/B RS on the casting component remains in a compressive stress state until it attains maximum CSD.

Additionally, Figure 12(B) reveals corresponding Von Mises and Tresca RSs on S/A and S/B cast product components within NCW at P1. It is illustrated that S/B casting component computed Von Mises and Tresca RSs are optimum near casting surfaces with measured magnitudes of approximately 328 and 378MPa and S/A casting component RSs measured at 164 and 180MPa at CSD of approximately 0.025mm, respectively. S/A and S/B cast product components computed RSs of Von Mises and Tresca rises and lessening, respectively, reaching RSs that are comparable in RS magnitudes at CSD of 0.075 and 0.175mm. Finally, computed RSs of Von Mises and Tresca rise to some extent linearly, reaching 429 and 474MPa at CSD of 0.275mm. Whereas S/B casting component computed Von Mises and Tresca RSs are lessening and revealing levels of variations of approximately 125 and 135MPa at CSD of approximately 0.275mm, respectively. Thus, it is noticed in Figure 12(B) that at a CSD of approximately 0.275mm, computed RSs of Von Mises and Tresca within the S/B casting component are retained to some extent, lessening linearly as the CSD rises. Whereas S/A casting component Von Mises and Tresca RSs are retained and rise as the CSD rises till it reaches optimum depth, it can be concluded that from Figure 12(B), RSs are relaxed and/or relieved within the S/B casting component as compared to the S/A casting component at P1 on NCW.

 doi:10.20944/preprints202505.0918.v1

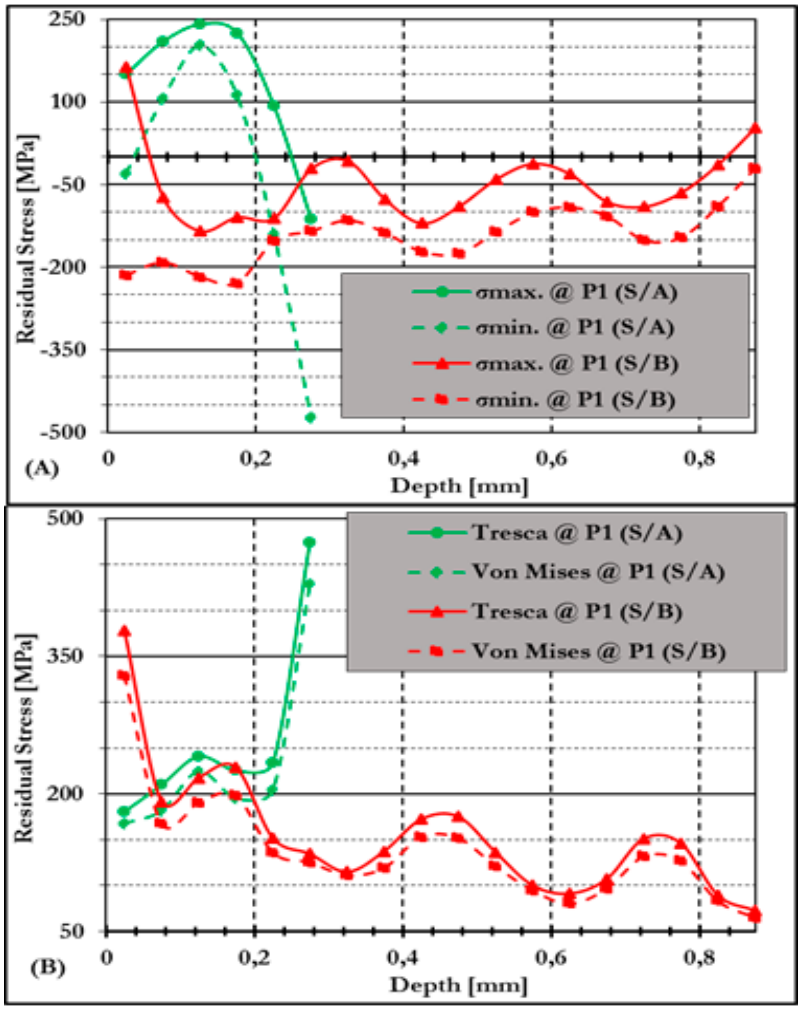

Figure 12. Evaluation regarding S/A vs. S/B-cast products within NCW at P1.

Residual Stresses at P2 of GCW on S/A and S/B

Measured RSs at P2 on GCW are compared between S/A and S/B casting components as presented in Figure 13 below in as-cast state. It is noticed in Figure 13(A) that RS state and distribution on both alloys, i.e., S/A and S/B alloys, respectively, are parallel "*alike.*". However, a noticeable variation is noticed in the RS magnitudes, especially near the casting surface and within the inner casting surface, as observed in Figure 13(A). Whereas near the casting surface, tensile stress states are noticed on both S/A and S/B casting components, with S/A cast products showing higher magnitudes. Furthermore, it is noticed in Figure 13(A) that the RS state is completely in a compressive stress state within the casting surfaces, whereas it is completely in a tension stress state near the casting surfaces and completely between a tension and compressive stress state at the maximum surface depth on both S/A and S/B cast components, respectively. Thus, RS on S/A and S/B cast products are increasing compressive stress state as the casting surface increases and reaching a completely compressive stress state within the inner layers.

S/A and S/B casting components near the casting surface, RS were measured at approximately 0.0255 and 0.01mm CSD with RS magnitudes of approximately 133 and 407MPa, -20 and 130MPa on $\sigma_{min.}$ and $\sigma_{max.}$ principal stresses, respectively. It is noticed on S/A and S/B cast products that there is an increase in compressive stress state as the casting depth increases, attaining -180 and -158MPa (0.125mm), -611 and -241MPa (0.31mm) on $\sigma_{min.}$ and $\sigma_{max.}$ principal stresses, respectively. In addition, S/A cast product RS state and distribution are noticed to some extent flattening and in steady tensile stress state up to CSD of approximately 0.875mm, thus attaining RSs of approximately 61 and 130MPa on $\sigma_{min.}$ and $\sigma_{max.}$ principal stresses, respectively. Whereas the S/B casting component RS state is

 doi:10.20944/preprints202505.0918.v1

displaying levels to some extent of fluctuations amongst CSD of approximately 0.59 and 0.69mm with RS measurements with magnitudes of approximately 70 and 23MPa, 51, and – 86MPa on $\sigma_{min.}$ and $\sigma_{max.}$ principal stresses, respectively. Lastly, S/B cast product RS stress states to some extent are flattening till the CSD of approximately 0.870mm with measured RS of approximately -22 and 6MPa on $\sigma_{min.}$ and $\sigma_{max.}$ principal stresses, respectively.

Von Mises and Tresca RSs shown in Figure (B) reveal that S/A casting component RSs are maximum as compared to S/B casting component near casting surfaces, thus reaching 140 and 149MPa, 359 and 407MPa, respectively, at approximately 0.025mm CSD. Whereas CSD rises, corresponding RSs reach 103 and 118MPa at approximately 0.075mm on Von Mises and Tresca RSs within the S/A casting component as compared to the S/B casting component reaching 82 and 90MPa at approximately 0.05mm CSD.

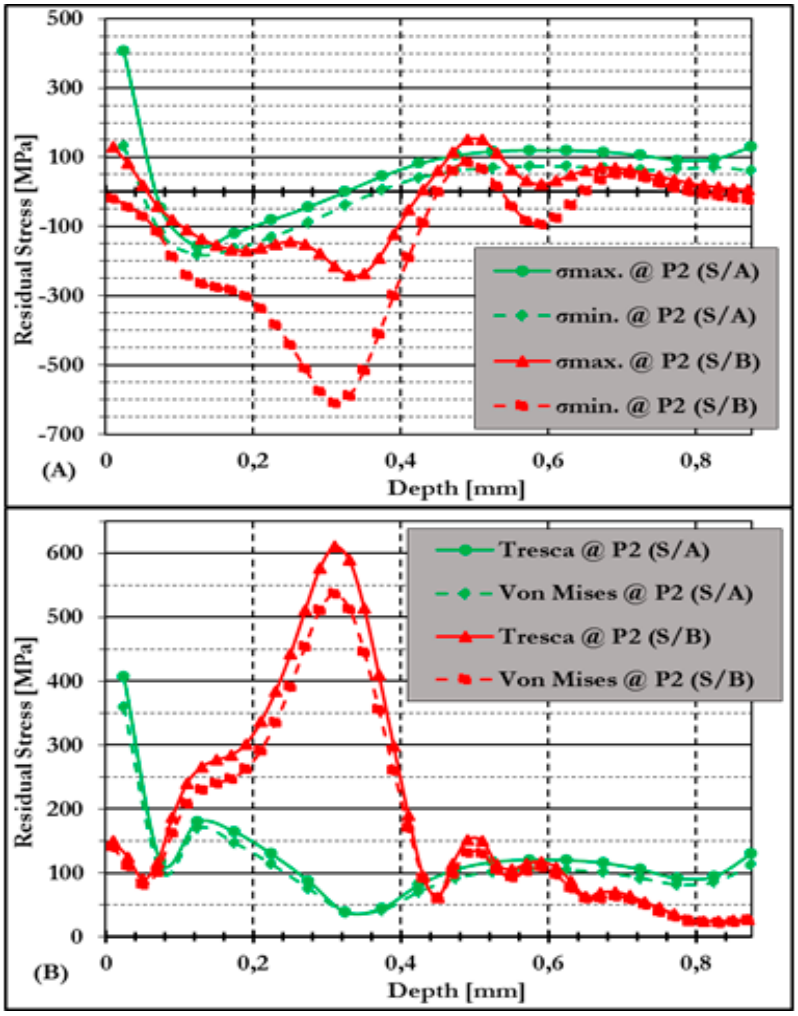

Figure 13. Evaluation regarding S/A vs. S/B-cast products within GCW at P2.

It is noticed in Figure 13(B) that RSs escalate to some extent as the CSD rises within the S/A casting component, reaching 170 and 180MPa at a CSD of approximately 0.125mm, afterwards lessening as the CSD rises, and revealing to some extent instabilities till the optimum CSD of approximately 0.875mm is reached with RS measurement measuring at approximately 112 and 130MPa on Von Mises and Tresca RSs, respectively. In addition, computed RSs within the S/B casting component, Von Mises and Tresca RSs, rise linearly with rising CSD, reaching extremely optimum RSs of approximately 536 and 611MPa at a CSD of approximately 0.31mm, afterwards lessening with rising CSD reaching at least RSs of approximately 61MPa with Von Mises and Tresca RSs. Whereas computed Von Mises and Tresca RSs within the S/B casting component rise to some extent, reaching

 doi:10.20944/preprints202505.0918.v1

132 and 151MPa at CSD of approximately 0.49mm, afterwards to some extent start to level till it reaches an optimum CSD of approximately 0.870mm with Von Mises and Tresca RSs reaching 23 and 28MPa, respectively. Thus, the established RSs at P2 on NCW reveal that RSs on hypoeutectic irons are comparable and only reveal variations in magnitudes. Whereas it can be concluded that the S/A casting component RS produces significantly minimum magnitudes of RSs as compared to the S/B casting component, which produces greater magnitudes of RSs distribution "*flow curves*" of compression state after shakeout at approximately 60 and 180°C, respectively.

Residual Stresses at P2 of NCW on S/A and S/B

Figure 14 below presents variations at P2 between S/A and S/B experimental casting, i.e., alloys on NCW. The S/A casting component presents higher magnitudes of RS as compared to the S/B casting component. However, S/A and S/B cast components were measured up to a surface depth of approximately 0.138 and 0.870mm, respectively. Near the surface, the measured RS were tensile stresses with approximately 427 and 534MPa at a surface depth of approximately 0.012mm of $\sigma_{min.}$ and $\sigma_{max.}$ principal stresses, respectively. S/A cast product RS increases in tensile stresses, thus reaching maximum magnitudes of approximately 665 and 958MPa at the surface depth of approximately 0.037mm. In addition, Figure 14(A) displays that as the surface depth increases on the S/A cast product, tensile stresses continue to increase in magnitude, thus reaching maximum magnitudes of approximately 705MPa of $\sigma_{max.}$ principal stresses at the surface of approximately 0.138mm, whereas compressive stresses were noticed to be approximately -105MPa of $\sigma_{min.}$ principal stresses.

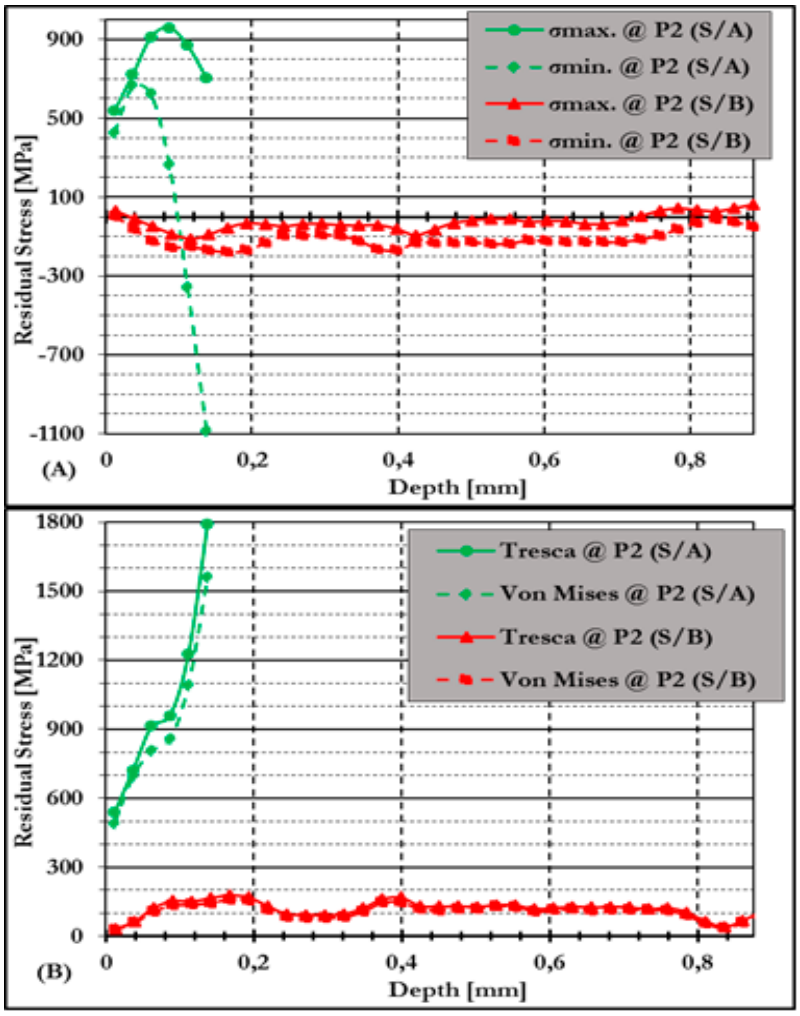

Figure 14. Evaluation on S/A and S/B cast products at P2 on NCW at P2.

 doi:10.20944/preprints202505.0918.v1

Furthermore, RS on S/B cast products as compared to S/A cast products was noticed in Figure 14(A) to be in a compressive steady state from the surface up to approximately 0.870mm. Whereas the minimum and maximum magnitude of fluctuation are measured at approximately -180 and 2MPa of $\sigma_{min.}$ and $\sigma_{max.}$ principal stresses, respectively, on the S/B cast product as shown in Figure 14(A). Thus, RS is higher in magnitudes on the S/A cast product as compared to the S/B cast product. Figure 14(B) reveals that Von Mises and Tresca RSs are maximum on S/A cast components as compared to S/B casting components. Whereas S/A Von Mises and Tresca RSs are rising linearly as the CSD increases, reaching optimum RSs between 492–1970MPa.

Furthermore, S/B casting component RSs, Von Mises, and Tresca are noticed to be stable and minimum, i.e., 150MPa within the inner CSD. Thus, it is concluded that in-cast state, RSs on NCW and GCW are established to relay on cooling rate during solidification and cooling stages "*periods*" and shakeout casting temperatures. While casting temperature during the shakeout process, rely on the cooling rate established during solidification and cooling periods, which are established to be significantly reliant on the shakeout period and/or time, respectively. Additionally, throughout the casting of casting components, liquid iron starts to be solid "*freeze*" over a temperature range due to hypoeutectic high-Cr irons. In addition, the liquid iron is freezing and transforming to solid iron, RSs starting to be established due to denser and crystalline regularity existing as atomic prearrangement that is held by strong interatomic binding forces as compared to the liquid iron state [68].

4. Conclusions

It was observed on the experimental castings shown above in Figures 1 and 2, respectively, such as S/A and S/B cast products, that tensile stresses were detected near the casting surface in as-cast environments "conditions," whereas in the internal layers, compressive stresses were detected as presented from Figures 3–14. This is due to outer layers solidifying at faster cooling rates, thus establishing a casting skin within the interface between the sand mould and the mushy metal at the core, thus leading to a fully tension state in the external layers and a compression state in the core, i.e., interior layers. Cores are normally solidifying last during solidification and cooling. Whereas the casting is still solidifying and cooling for a determined period. The feeder "riser" feeding of the casting component during solidification, the mushy metal when solidifying, pulls away from the sand mould.

In addition, during solidification of the casting core, inner and outer layers experience compression "contraction" and tension "pulling," respectively. For many years, experimental and numerical models for analysing mechanical components, i.e., casting/s on performance and design, have been widely used in industry. Thus, the results will lead to an improved design through the offering of beneficial understandings into critical areas of the casting during use "operation" and an enhancement of product quality. Removal of junk material from the NCW led to the introduction and alteration of RSs on the casting component, whereas GCW RSs were introduced through solidification and cooling processes, leading to variations in thermal gradients. Thus, RSs were detected on GCW after shakeout at different temperatures, i.e., 60 and 180°C, respectively.

There is no direct correlation between time and direct influence within the mechanical model, only indirect loading via thermal gradient. On the mechanical model, time has no direct impact, only indirect impact on the loading through thermal gradients. Time only starts to have impact and play a significant part directly when cooling is slow or fast. Cooling fast led to conditions equivalent to the quenching process, whereas the cast product response is delicate to the strain degree, i.e., the response becomes viscoplastic as an alternative to plastic. Whereas cooling sluggishness led to circumstances observed in general heavy casting components, where thermal slopes "*gradients*" are minimum and cooling time "*period*" is more than enough for lessening of RSs to take place. Thus, time dependency is defined through creep, whereas inelastic strain degree is correlated to RS stages "*levels*" [70]. Elevated varieties of material properties are observed after casting processes.

Dimensional stability of the metallic "*casting*" component is influenced by major factors during casting processes. These are the steadiness of the micrographs "*microstructural evaluations*" and the

 doi:10.20944/preprints202505.0918.v1

regulators of the RS during cast products heat treatment processes [63]. Furthermore, hardness measurements established are higher than estimated hardness values from the ASTM A532 standard. This increase, such as 526 and 600HBN in hardness values as per ASTM A532, i.e., 450BHN [14], can be encouraged by casting shakeout temperatures, i.e., 60 and 180°C compared to normal as-cast ambient temperatures. Through shakeout processes, RS have a noticeable significance on the methods; the cast product twists "distorts" through solidification and cooling, respectively, to room temperatures. Thus, the following are conclusions that are based on the study findings, *viz*.:

(1) Higher casting shakeout temperatures encourage optimum hardness values.
(2) Non-uniform RS distribution is normally detected.
(3) Thinner casting section thickness led to minimum magnitudes of RSs as compared to thicker section thickness, which introduced optimum RS magnitudes.
(4) Separating and/or removing junk material from NCW led to a modification of RS state.
(5) RSs within NCW are forever in the opposite direction of the GCW RS distribution.
(6) Castings shakeout at elevated temperatures led to advanced tensile RSs.
(7) Shakeout at elevated temperatures led to steady compressive RSs on NCW.

5. Future Work

To progress the consideration of RSs on casting components of HCWCI alloys, i.e., hypoeutectic and eutectic irons before and after removal of junk material after casting knock-off processes, the investigation studies can be sustained to validate through measuring more than ten casting components for validation purposes. While modelling of RSs before and after removal of junk material can be investigated further. Lastly, various RS measurements on HCWCI alloys can be investigated further to improve manufacturing process design and reduce scrap rate, which is related to RS and distortion casting defects. Since the present research study only focused on both gross and net casting components as compared to heat-treated and machined casting processes. While further focusing on before and after heat treatment and machining processing RS measurement during casting design.

Acknowledgments: The study was performed in South Africa (SA) at the University of Johannesburg (UJ) in the Department (Dep.) of Engineering Metallurgy. The author requests to show gratitude to the succeeding organisations and institutions that made it possible for this study: South African government organisations, such as the National Research Foundation (NRF), the Department of Trade and Industry (DTI), the National Foundry Technology Network (NFTN), the Department of Science and Technology (DST), and Mintek. Whereas private sector contributions that are acknowledged are Mitak Foundries (Pty) Ltd, Ametex (Pty) Ltd, and Scaw Metals SA for the research funding. In addition, Ametex (Pty) Ltd, Mintek, and Mitak Foundries (Pty) Ltd. are extremely cherished for allowing the use of their facility and equipment. Whereas for RS measurements, Wits University School of Mechanical, Industrial, and Aeronautical Engineering is highly treasured for allowing use of their facilities, i.e., the laboratory.

References

1. Oh, J.-S., Song, Y.-G., Choi, B.-G., Bhamornsut, C., Nakkuntod, R., Jo, C.-Y. & Lee, J.-H., 2021. Effect of Dendrite Fraction on the $M_{23}C_6$ Precipitation Behavior and the Mechanical Properties of High Cr White Irons. *Multidisciplinary Digital Publishing Institute (MDPI),* 3 October, 11(1576), p. 19.
2. Fashu, S. & Trabadelo, V., 2023. Development and Performance of High Chromium White Cast Irons (HCWCIs) for Wear-Corrosive Environments: A Critical Review. *Metals,* 13(1831), pp. 1–26.
3. Zhang, Y., Shimizu, k., Yaer, X., Kusumoto K. & Efremenko, V. G., 2017. Erosive Wear Performance of Heat Treated Multi-Component Cast Iron Containing Cr, V, Mn and Ni Eroded by Alumina Spheres at Elevated Temperatures. *Wear,* pp. 1–20.
4. Islak, S., Ozorak, C., Kir, D., Kucuk, O., Akkas, M. & Sezgin, C. T., 2015. *The Effect of Different Carbon Content on the Microstructural Characterization of High Chromium White Cast Irons.* Karabuk, Turkey, s.n., p. 4.

 doi:10.20944/preprints202505.0918.v1

5. Li, H., Zhuang, M., Li, C., Wu, S. & Rong, S., 2018. Effect of Carbon Element Change on Microstructure and Properties of Fe-Cr-C Surfacing Alloy. *Earth and Environmental Science,* Volume 186, p. 6.
6. Tian, Y., Ju, J., Fu, H., Shengqiang M. S., Lin, J. & Lei, Y., 2019. Effect of Chromium Content on Microstructure, Hardness, and Wear Resistance of As-Cast Fe-Cr-B Alloy. *Journal of Materials Engineering and Performance,* p. 11.
7. Ngqase, M. Nheta, W., Madzivhandila, T., Phasha, M. & Pan, X., 2024. Exploring Residual Stress Analysis in the Machining of Hypoeutectic High Chromium White Cast Iron Alloys Through the Hole-Drilling Method. *Engineering Research Express,* 6(045414), pp. 1–19.
8. Mabeba, A. D., 2021. *Development of High Vanadium Grinding Media Materials for the Comminution of Gold Ore,* Pretoria, Republic of South Africa: University of Pretoria.
9. Moema, J. S., 2018. *The Role of Retained Austenite on the Performance of High Chromium White Cast Iron and Carbidic Austempered Nodular Iron for Grinding Ball Applications,* Pretoria, Republic of South Africa: University of Pretoria.
10. Ngoc, Q. H. T., Diem, N. T. V., Hoang, V. N., Hong, H. N., Thu, H. L. & Duong, N. N., 2022. Effect of Residual Stress Distribution on the Formation, Growth and Coalescence of Voids of 27Cr White Cast Iron Under Impact. 63(2), pp. 170–175.
11. Motsumi, V. M., 2021. *Investigation of the Micro- and Macroscopic Wear Properties of Cemented Tungsten Carbide for the Wear Lining Material Selection of Chutes,* Johanneburg: s.n.
12. Ngqase, M. & Pan, X., 2019. *Microstructural Investigation on Heat Treatment of Hypoeutectic High.* s.l., IOP Publishing, p. 12.
13. Tupaj, M., Orłowicz, A. W., Trytek, A., Mróz, M., Wnuk, G. & Dolata, A. J., 2020. The Effect of Cooling Conditions on Martensite Transformation Temperature and hardness of 15%Cr Chromium Cast Irons. *Materials,* 13(2760), p. 13.
14. Ngqase, M., 2018. *Validation of Physical Properties of HCWCI Alloys Towards Comprehensive Process Simulation Capabilities,* Doorfontein, Johannesburg, South Africa: University of Johannesburg.
15. Baghani, A., Davami, P., Varahram, N. & Shabani, M. O., 2014. Investigation on the Effect of Mold Constraints and Cooling Rate on Residual Stress During the Sand-Casting Process of 1086 Steel by Employing a Thermomechanical Model. *Metallurgical and Materials Transactions B,* p. 13.
16. Elmquist, L., Brehmer, A., Schmidt, P. & Israelsson, B., 2018. Residual Stresses in Cast Iron Components—Simulated Results Verified by Experimental Measurements. *Material Science Forum,* Volume 925, pp. 326–333.
17. Chaudry, U. M., Tekumalla, S., Gupta, M., Jun, T. -S. & Hamad, K., 2022. Designing Highly Ductile Magnesium Alloys: Current Status and Future Challenges. *Critical Reviews in Solid State and Materials Sciences,* 47(2), pp. 194–281.
18. Egan, P. F., 2023. Design for Additive Manufacturing: Recent Innovations and Future Directions. *Design,* 7(83), p. 32.
19. Samuel, E., Samuel, A. M., Songmene, V. & Samuel, F. H., 2023. A Review on the Analysis of Thermal and Thermodynamic Aspects of Grain Refinement of Aluminum-Silicon-Based Alloys. *Materials,* 16(5639), p. 29.
20. Nemyrovskyi, Y., Shepelenko, I. & Storchak, M., 2023. Plasticity Resource of Cast Iron at Deforming Broaching. *Metals,* 13(551), p. 19.
21. Gong, L., Fu, H. & Zhi, X., 2023. Corrosion Wear of Hypereutectic High Chromium Cast Iron: A Review. *Metals,* 13(308), p. 21.
22. Akhtar, R. A., 2017. *A Study of Residual Stresses in Low Alloy Steel Theta Ring Casting,* Sheffield, South Yorkshire, England: ProQuest.
23. Yang, Y., 2020. *Development of a Method to Measure Residual Stresses in Cast Components with Complex Geometries,* Stockholm, Sweden: KTH.
24. Torres, I. N., Gilles, G., Tchuindjang, J. T., Lecomte-Beckers, J., Sinnaeve, M. & Habraken, A. M., 2014. Study of Residual Stresses in Bimetallic Work Rolls. *Advanced Materials Research,* Volume 996, pp. 580–585.

 doi:10.20944/preprints202505.0918.v1

25. Alipooramirabad, H., Kianfar, S., Paradowska, A. & Ghomashchi, R., 2024. Residual Stress Measurement in Engine Block—An Overview. *The International Journal of Advanced Manufacturing Technology,* Volume 131, pp. 1–27.
26. Tabatabaeian, A., Ghasem, H. R., Shokrieh, M. M., Marzbanrad, B., Baraheni, M. & Fotouhi, M., 2022. Residual Stress in Engineering Materials: A Review. *Advanced Engineering Materials,* 24(2100786), p. 28.
27. Akhtar, W., Lazoglu, I. & Liang, S. Y., 2022. Prediction and Control of Residual Stress-Based Distortions in the Machining of Aerospace Parts: A Review. *Journal of Manufacturing Processes,* Volume 76, pp. 106–122.
28. Qutaba, S., Asmelash, M., Saptaji, K. & Azhari, A., 2022. A Review on Peening Processes and its Effect on Surfaces. *The International Journal of Advanced Manufacturing Technology,* 120, Volume 120, pp. 4233–4270.
29. Franceschi, A., Stahl, J., Kock, C., Selbmann, R., Ortmann-Ishkina, S., Jobst, A., Merklein, M., Kuhfuß, B., Bergmann, M., Behrens, B. -A., Volk, W. & Groche, P., 2021. Strategies for Residual Stress Adjustment in Bulk Metal Forming. *Archive of Applied Mechanics,* Volume 91, pp. 3557–3577.
30. Hayama, M., Kikuchi, S., Tsukahara, M. & Misaka, Y., 2024. Estimation of Residual Stress Relaxation in Low Alloy Steel with Different Hardness during Fatigue by in Situ X-Ray Measurement. *International Journal of Fatigue,* Volume 178, pp. 1–11.
31. Bastola, N., Jahan, M. P., Rangasamy, N. & Rakurty, C. S., 2023. A Review of the Residual Stress Generation in Metal Additive Manufacturing: Analysis of Cause, Measurement, Effects, and Prevention. *Micromachines,* 14(1480).
32. Ammar, M. M. A. & Shirinzadeh, B., 2022. Evaluation of Robotic Fiber Placement Effect on Process-Induced Residual Stresses Using Incremental Hole-Drilling Method. *Polymer Composites,* Volume 43, pp. 4417–4436.
33. Yesudhas, S., Levitas, V. I., Lin, F., Pandey, K. K., & Smith, J. S., 2024. Unusual Plastic Strain-Induced Phase Transformation Phenomena in Silicon. *Article,* 15(7054), p. 13.
34. Mohamed, S. S., Samuel, A. M. & Samuel, F. H., 2018. Development of Residual Stresses in Al–Si Engine Blocks Subjected to Different Metallurgical Parameters. *International Journal of Metal Casting,* p. 13.
35. Nenchev, B., 2020. *Modeling and Analysis of Solidification Shrinkage and Defect Prediction in Metals,* Leicester, England: s.n.
36. Soar, P., Kao, A., Djambazov, G., Shevchenko, N., Eckert, S. & Pericleous, K., 2020. The Integration of Structural Mechanics into Microstructure Solidification Modelling. *Materials Science and Engineering,* Volume 861, p. 9.
37. Wang, G.-H. & Li, Y.-X., 2020. Thermal conductivity of cast iron—A Review. *Special Review,* 17(2), pp. 85–95.
38. Malik, I., Sani, A. A. & Medi, A., 2020. Study on using Casting Simulation Software for Design and Analysis of Riser Shapes in a Solidifying Casting Component. *Journal of Physics: Conference Series,* Volume 1500, pp. 1–7.
39. Pant, G., Reddy, M. S. S., Praveen, Parashar, A. K., Kareem, S. A. & Nijhawan, G., 2023. Advanced Casting Techniques for Complex-Shaped Components: Design, Simulation and Process Control. *ICMPC,* Volume 430, pp. 1–10.
40. Donghong, W., Yu, J., Yang, C., Hao, X., Zhang, L. & Peng, Y., 2022. Dimensional Control of Ring-to-Ring Casting with a Data-Driven Approach During Investment Casting. *The International Journal of Advanced Manufacturing Technology,* Volume 119, pp. 691–704.
41. Prikhod'ko, O. G., Deev, V. B., Prusov, E. S. & Kutsenko, A. I., 2020. Influence of Thermophysical Characteristics of Alloy and Mold Material on Casting Solidification Rate. *Steel in Translation,* 50(5), pp. 296–302.
42. Xu, J., Kang, J., Shangguan, H., Deng, C., Hu, Y., Yi, J. & Mao, W., 2022. Chimney Structure of Hollow Sand Mold for Casting Solidification. *Metals,* 12(415), p. 17.
43. Gurusamy, P., Bhattacharjee, B., Dutta, H. & Bhowmik, A., 2024. Study of Microstructural, Machining and Tribological Behaviour of AA-6061/SiC MMC Fabricated Through the Squeeze Casting Method and Optimized the Machining Parameters by Using Standard Deviation-PROMETHEE Technique. *Silicon,* Volume 16, pp. 675–686.
44. Zhiguo, Z., Chengkai, Y., Peng, Z. & Wei, L., 2014. Microstructure and Wear Resistance of High Chromium Cast Iron Containing Niobium. *Reaserch & Development,* May, 11(3), pp. 179–184.

 doi:10.20944/preprints202505.0918.v1

45. Lundberg, M. & Elmquist, L., 2018. *Hole Drilling Residual Stress Evaluations in Cast Iron.* Jönköping, Sweden, ECRS-10, pp. 89–94.
46. Venu, B. & Ramachandra, R., 2017. Simulation of Residual Stresses in Castings. *International Journal of Scientific Research in Science and Technology,* 3(8), pp. 875–890.
47. Demirer, E., Pourasiabi, H. & Gates, J. D., 2022. Effects of Particle Impingement and Coarse Particle Abrasion on Wear Performance of White Cast Irons in Sliding Bed Applications. *Society of Tribologists and Lubrication Engineers,* pp. 1–16.
48. Duflou, J. R., Wegener, K., Tekkaya, A. E., Hauschild, M., Bleicher, F., Yan, J. & Hendrickx, B., 2024. Efficiently Preserving Material Resources in Manufacturing: Industrial Symbiosis Revisited. *CIRP Annals-Manufacturing Technology,* Volume 73, pp. 695–721.
49. Alsaihati, A. & Elkatatny, S., 2023. A New Method for Drill Cuttings Size Estimation Based on Machine Learning Technique. *Arabian Journal for Science and Engineering,* Volume 28, pp. 16739–16751.
50. Sivan, S. S. S., Mrinal, B. D. J., Natarajan, S. & Chauhan, N., 2018. Analysis of Residual Stresses, Thermal Stresses, Cutting Forces and other Output Responses of Face Milling Operations on ZE41 Magnesium Alloy. *International Journal of Modern Manufacturing Technologies,* X(1), pp. 92–100.
51. Schröder, J., Evans, A., Mishurova, T., Ulbricht, A., Sprengel, M., Serrano-Munoz, I., Fritsch, T., Kromm, A., Kannengießer, T. & Bruno, G., 2021. Diffraction-Based Residual Stress Characterization in Laser Additive Manufacturing of Metals. *Metals,* 11(1830), p. 34.
52. Mohsen, S. & Behrooz, A., 2022. A Review in Machining-Induced Residual Stress. 12(1), pp. 64–68.
53. Guo, J., Fu, H., Pan, B. & Kang, R., 2021. Recent Progress of Residual Stress Measurement Methods: A Review. *Chinese Journal of Aeronautics,* 34(2), pp. 54–78.
54. Chiu, S. M.; Wu, C. Y.; Chuang, T. L.; Wang, K. K.; Ma, N. Y., 2015. *The Microstructure and Residual Stress Analysis of Gray Casting by Ultrasonic Technique.* Taipei, Taiwan, s.n., pp. 1–5.
55. Mehr, F. F., Cockcroft, S. & Maijer, D., 2020. A Fully-Coupled Thermal-Stress Model to Predict the Behavior of the Casting-Chill Interface in an Engine Block Sand Casting Process. *International Journal of Heat and Mass Transfer,* Volume 152, pp. 1–15.
56. Andriollo, T., Hellström, K., Sonne, M. R., Thorborg, J., Tiedje, N. & Hattel, J., 2018. Uncovering the Local Inelastic Interactions during Manufacture of Ductile Cast Iron: How the Substructure of the Graphite Particles can Induce Residual Stress Concentrations in the Matrix. *Journal of the Mechanics and Physics of Solids,* Volume 111, pp. 333–357.
57. Smit, T. C., Nobre, J. P., Reid, R. G., Wu, T., Niendorf, T., Marais, D. & Venter, A. M., 2022. Assessment and Validation of Incremental Hole-Drilling Calculation Methods for Residual Stress Determination in Fiber-Metal Laminates. *Advances in Residual Stress Technology,* Volume 62, pp. 1289–1304.
58. Barile, C., Casavola, C., Pappalettera, G. & Pappalettere, C., 2014. Remarks on Residual Stress Measurement by Hole-Drilling and Electronic Speckle Pattern Interferometry. *The Scientific World Journal,* Volume 2014, pp. 1–7.
59. Ngqase, M. & Pan, X., 2020. An Overview on Types of White Cast Irons and High Chromium White Cast Irons. *International Conference on Multifunctional Materials (ICMM-2019)–Journal of Physics: Conference Series,* p. 13.
60. Ngqase, M. & Pan, X., 2020. *XRD Investigation on Heat Treatment of High Chrome White Cast Irons.* s.l., IO Pushiling, p. 11.
61. Seidu, S. O., Oloruntoba, D. T. & Otunniyi, I. O., 2014. Effect of Shakeout Time on Microstructure and Hardness Properties of Grey Cast Iron. *Journal of Minerals and Materials Characterization and Engineering,* Volume 2, pp. 346–350.
62. Borle, S. D., 2014. *Microstructural Characterisation of Chromium Carbide Overlays and a Study of Alternative Welding Processes for Industrial Wear Applications,* Admonton, Alberta: Spring.
63. Zhang, Y. B., Andriollo, T., Fæster, S., Liu, W., Hattel, J. & Barabash, R. I., 2016. Three-Dimensional Local Residual Stress and Orientation Gradients Near Graphite Nodules in Ductile Cast Iron. *Acta Materialia,* Volume 121, pp. 173–180.

 doi:10.20944/preprints202505.0918.v1

64. Milenin, A., Kustra, P., Kuziak, R. & Pietrzyk, M., 2014. Model of Residual Stresses in Hot-Rolled Sheets with Taking into Account Relaxation Process and Phase Transformation. *Procedia Engineering,* Volume 81, pp. 108–113.
65. Song, J., Huang, Y., Gan, W. & Hort, N., 2014. Residual Stresses of the As-Cast Mg-xCa Alloys with Hot Sprues by Neutron Diffraction. *Advanced Materials Research,* Volume 996, pp. 592–597.
66. Keste, A. A., Gawande, H. S. & Sarkar, C., 2016. Design Optimization of Precision Casting for Residual Stress Reduction. Volume 3, pp. 140–150.
67. Feng, Q., Zeng, Y., Li, J., Wang, Y., Tang, G. & Wang, Y.,, 2024. Effect of Carbides on Thermos-Plastic and Crack Initiation and Expansion of High-Carbon Chromium-Bearing Steel Castings. *Metals,* 14(335), pp. 1–19.
68. Li, X., Liu, J., Wu, H., Miao, K., Wu, H., & Li, R., 2024. Review Article: Research Progress of Residual Stress Measurement Methods. *Heliyon 10 (2024) e28348,* 10(e28348), pp. 1–25.
69. Sroka, J., 2021. *Residual Stresses in lLarge Sizes Forgings,* Sheffield, England: s.n.
70. Lundberg, M., 2018. *Residual Stresses, Fatigue and Deformation in Cast Iron,* s.l.: LiU-Tryck.